Parameter Identification of PEMFC via Feedforward Neural Network-Pelican Optimization Algorithm

Bo Yang[a], Boxiao Liang[a], Yucun Qian[a], Ruyi Zheng[a], Shi Su[b], Zhengxun Guo[c, d *], Lin Jiang[e]

[a] Faculty of Electric Power Engineering, Kunming University of Science and Technology, 650500 Kunming, China;

[b] Power Science Research Institute of Yunnan Power Grid Co., Ltd, 650217 Kunming, China;

[c] College of Information Science and Engineering, Northeastern University, 110819 Shenyang, China;

[d] Foshan Graduate School of Innovation, Northeastern University, 528311 Foshan, China;

[e] Department of Electrical Engineering & Electronics, University of Liverpool, Liverpool L69 3GJ, United Kingdom.

[*] Corresponding author: Zhengxun Guo, E-mail: ZhengxunGuo@outlook.com

Abstract: Parameter identification is a critical task in the research of proton exchange membrane fuel cells (PEMFC), which provides the basis for establishing an accurate and reliable PEMFC model. However, the nonlinear characteristics of PEMFC model as well as inevitable noise data and insufficient measurement data often overwhelm traditional optimization techniques. In particular, noise data and inadequate measurement data can introduce bias or lead to data loss. To address this problem, a novel hybrid optimization strategy is proposed. Firstly, a feedforward neural network (FNN) is employed to preprocess the measured data (i.e., reducing noise data and enriching measurement data). Furthermore, Gaussian noise and Rayleigh noise with three signal-to-noise ratio levels are introduced to simulate various disturbances of noise. Then, the pelican optimization algorithm (POA) is used to identify the parameters of PEMFC based on preprocessed data. Lastly, the effectiveness of the proposed strategy named FNN-POA is verified by comparing it with seven advanced competitive algorithms. Simulation results demonstrate that FNN-POA has higher robustness and optimization quality by comparing original data and preprocessed data. For instance, the root-mean-square error obtained by FNN-POA is reduced by 99.44% under medium temperature and medium pressure through noise reduction.

Keywords: PEMFC, FNN, POA, parameter identification, data noised reduction, data prediction.

Nomenclature			
Variables		IMOA	improved monarch optimization algorithm
$\varepsilon_1, \varepsilon_2, \varepsilon_3,$	semi-empirical coefficients	IWOA	improved whale optimization algorithm
λ	the water content of the membrane	JS	artificial jellyfish search algorithm
R_c	membrane equivalent resistance, Ω	LSTM	long short term memory
b	parameter coefficient, V	LTHP	low temperature and high pressure
Abbreviations		MCFC	molten carbonate fuel cell
AFC	alkaline fuel cell	MFO	moth-flame optimization
ASSA	adaptive sparrow search algorithm	MhAs	meta-heuristic algorithms
BMO	bird mating optimizer	MTMP	medium temperature and medium pressure
BP	back propagation	MVO	multi-verse optimizer
CL	catalyst layer	PAFC	phosphate acid fuel cell
FF	flow field	PEM	proton exchange membrane

FNN	feedforward neural network	PEMFC	proton exchange membrane fuel cell
FNN-POA	POA based on FNN	POA	pelican optimization algorithm
GBO	gradient-based optimizer	PSO	particle swarm optimization
GDL	gas diffusion layer	RMSE	root mean square error
GRNN	general regression neural network	SD	standard deviation
GWO	grey wolf optimization	SOFC	solid oxide fuel cell
HBO	honey badger optimizer	SNR	signal-to-noise ratio
HHO	Harris hawk optimization	TLBO	teaching-learning-based optimization
HTLP	high temperature and low pressure	*V-I*	voltage-current

1. Introduction

Ecological and environmental protection and sustainable development of the world are mutually reinforcing [1]. Nowadays, serious environmental degradation, growing energy demand, and the depletion of traditional fossil fuel resources pose a great challenge to the world's sustainable development [2]. To cope with these challenges, the optimization of the energy structure and the energy revolution have become indispensable. The development and utilization of renewable energy, e.g., solar energy [3], wind energy [4], and hydrogen energy [5] can solve environmental and energy problems. Upon which the hydrogen fuel cell has attracted the attention of many countries thanks to its advantages, i.e., high fuel energy conversion and zero emission. According to the different types of electrolytes, it can be divided into alkaline fuel cell (AFC) [6], phosphate acid fuel cell (PAFC) [7], proton exchange membrane fuel cell (PEMFC) Error: Reference source not found, molten carbonate fuel cell (MCFC) [8] and solid oxide fuel cell (SOFC) [10], upon which PEMFC enjoys rapid development and wide application due to low operating temperature.

PEMFC was first applied in aerospace, military equipment, and other fields [11]. With the reduction of production costs and the rapid development of related technologies, PEMFC has formed a certain market scale in transportation, portable power supply, and other fields [12]. However, to realize large-scale commercialization of PEMFC, further research is still required to improve the performance of PEMFC and extend its service life. Note that PEMFC modeling has become the key and foundation to study the above problems. Based on modeling methods, it can be classified into four categories: mechanism model [13], semi-empirical model [14], empirical model [15], and data-driven model [16]. The electrochemical model based on a semi-empirical model has been widely used because of its precise characteristic expressiveness in the reaction process and adaptiveness in different operating conditions.

Nevertheless, parameter identification of the electrochemical model is a complicated nonlinear problem with high modal cells, and it is difficult to use traditional numerical analysis methods to identify parameters. Fortunately, numerous MhAs have been used to extract unknown parameters of PEMFC [17] thanks to their low requirement of initial value and global search ability. For example, particle swarm optimization (PSO) [18] was applied to improve the parameter identification accuracy. Reference [19] proposed a parameter identification scheme based on a gradient-based optimizer (GBO), which showed satisfactory

global optimization ability on different brands of PEMFC. In addition, other original MhAs also achieved high-quality solutions, e.g., artificial jellyfish search algorithm (JS) [20], multi-verse optimizer (MVO) [21], bird mating optimizer (BMO) Error: Reference source not found and honey badger optimizer (HBO) [22], etc. Furthermore, various hybrid and improved algorithms were also developed and applied. For instance, an adaptive sparrow search algorithm (ASSA) [24] was designed for different PEMFCs from different manufacturers, upon which adaptive learning factors were introduced to enhance accuracy. Similarly, an improved monarch optimization algorithm (IMOA) was constructed to improve the accuracy and convergence speed by referring to chaotic local search and establishing a quasi-opposition mechanism in reference [25].

While MhAs have acquired impressive identification results based on ideal and conventional data, the real measurement data offered by manufacturers sometimes may be insufficient and even noised due to data loss and the interruption of the collection instrument, various operating environmental disturbances, etc., which may greatly damage the identification performance of them. Aiming at this obstacle, this paper proposes a hybrid optimization scheme to identify the unknown parameters of PEMFC, namely a feedforward neural network based on pelican optimization algorithm (FNN-POA). It owns the following four contributions:

- FNN based data preprocess model, which is compared with other three efficient neural networks under different operating conditions, is subtly and reasonably established to denoise and extend *V-I* data of PEMFC, thus servicing for decreasing the influence of noised data and insufficient data on identification results;
- Two kinds of white noise (i.e., Gaussian white noise and Rayleigh white noise) and three different levels of noise are adopted to simulate the effect of real noise on PEMFC, thus fully evaluating the superiority of FNN in data noise reduction;
- Pelican optimization algorithm (POA) is applied to identify the unknown parameters of PEMFC model and thoroughly compared with seven competitive algorithms from three aspects, i.e., accuracy, speed, and stability;
- Comprehensive and profound case studies are designed to evaluate and analyze the effectiveness and feasibility of FNN-POA under three operating conditions, i.e., high temperature and low pressure (HTLP), medium temperature and medium pressure (MTMP), and low temperature and high pressure (LTHP).

2. PEMFC modeling

2.1 The theory of PEMFC

The basic components of a proton exchange membrane fuel cell include proton exchange membrane (PEM), gas diffusion layer (GDL), catalyst layer (CL), and flow field (FF). In the power generation process, the basic reaction mechanism diagram is shown in Fig. 1. Hydrogen is decomposed into hydrogen ions and electrons at the anode, upon which the hydrogen ions and the electrons are transferred to the cathode through PEM and load, respectively. Then, the hydrogen ions and electrons react with the oxygen in the cathode to produce heat and water

[26].

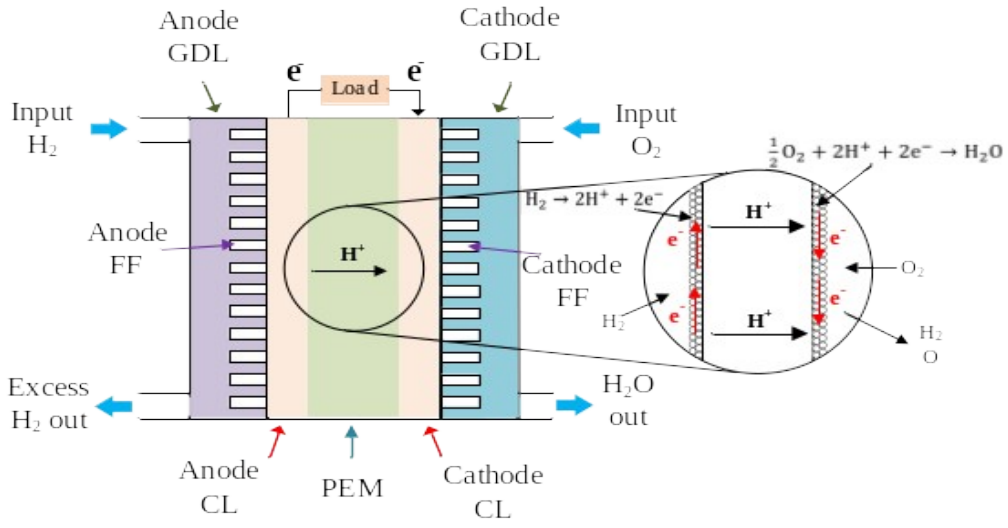

Fig. 1. PEMFC reaction mechanism diagram.

Overall, the reaction mechanism of PEMFC can be summarized by Eqs. (1)-(3), as follows:

The reaction equation on the anode:

$$H_2 \rightarrow 2H^{+} + 2e^{-} \quad (1)$$

The reaction equation on the cathode:

$$\frac{1}{2}O_2 + 2H^{+} + 2e^{-} \rightarrow H_2O \quad (2)$$

Overall reaction mechanism equation:

$$H_2 + \frac{1}{2}O_2 \rightarrow H_2O \quad (3)$$

2.2 Mathematical model of PEMFC

In the operation process, the potential of PEMFC will gradually decrease, because there is an irreversible loss in the cell, known as the polarization potential. As shown in Fig. 2, the polarization curve of PEMFC is mainly affected by the polarization potential of three parts, i.e., activation polarization, ohmic polarization, and concentration polarization [27].

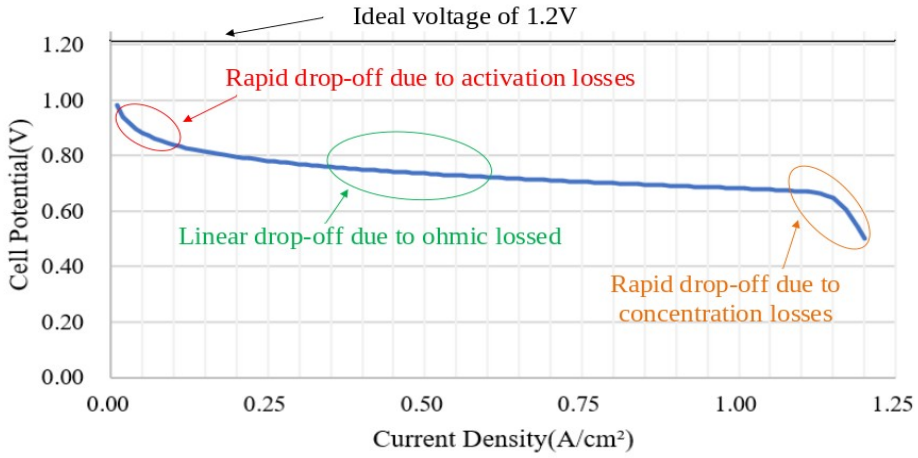

Fig. 2. The typical polarization curve of the PEMFC.

Considering the impact of polarization potential in electrochemical reactions of PEMFC, the output voltage of a single cell can be described by [28]

$$V_{est} = E_{nernst} - V_{act} - V_{ohm} - V_{con} \tag{4}$$

where V_{act}, V_{ohm} and V_{con} individually represent activation voltage loss, ohmic voltage loss, and concentration voltage loss; E_{nernst} is the thermodynamic electromotive force, which can be written as [28]

$$E_{nernst} = \frac{\Delta G}{2F} + \frac{\Delta S}{2F} \times (T - T_{ref}) + \frac{RT}{2F} \times \left[\ln(P_{H_2}) + \frac{1}{2} \ln(P_{O_2}) \right] \tag{5}$$

where ΔG represents change in free Gibbs energy; ΔS stands for change in entropy; F denotes the Faraday constant; R is the universal gas constant; T and T_{ref} represent the actual temperature and reference temperature in Kelvin, respectively; P_{H_2} and P_{O_2} denote the partial pressure of hydrogen and oxygen, which can be calculated by

$$P_{H_2} = 0.5 \times RH_a \times P_{H_2O}^{sat} \times \left[\left(\frac{RH_a \times P_{H_2O}^{sat}}{P_a} \times \exp\left(\frac{1.635 \times \left(\frac{i_{cell}}{A} \right)}{T^{1.334}} \right) \right)^{-1} - 1 \right] \tag{6}$$

$$P_{O_2} = RH_c \times P_{H_2O}^{sat} \times \left[\left(\frac{RH_a \times P_{H_2O}^{sat}}{P_c} \times \exp\left(\frac{4.192 \times \left(\frac{i_{cell}}{A} \right)}{T^{1.334}} \right) \right)^{-1} - 1 \right] \tag{7}$$

where RH_a and RH_c are the relative humidity of the vapor in the anode and cathode, respectively; P_a and P_c stand for the entrance pressure of the anode and cathode, individually; i_{cell} is defined as the output current of a single cell; A represents the effective activation area of PEM; $P_{H_2O}^{sat}$ denotes the saturation pressure of water vapor, which can be expressed as [29]

$$\log_{10}(P_{H_2O}^{sat}) = 2.95 \times 10^{-2} \times T_c - 9.19 \times 10^{-5} \times T_c^2 + 1.44 \times 10^{-7} \times T_c^3 - 2.18 \tag{8}$$

$$T_c = T - 273.15 \tag{9}$$

Besides, the activation voltage loss V_{act} can be calculated as

$$V_{act} = -¿¿ \quad (10)$$

where ε_1, ε_2, ε_3, and ε_4 are semi-empirical coefficients; C_{O_2} denotes the concentration of oxygen catalyzed by the anode catalyst surface, which can be formulated by

$$C_{O_2} = \frac{P_{O_2}}{5.08 \times 10^6 \times e^{\left(\frac{-498}{T}\right)}} \quad (11)$$

Besides, the ohmic voltage loss V_{ohm} can be calculated by [29]

$$V_{ohm} = i_{cell} \times \left(R_m + R_c\right) \quad (12)$$

where R_c denotes the proton exchange membrane equivalent resistance; R_m is the electron transfer resistance, which is determined as

$$R_m = \rho_m \times \left(\frac{l}{A}\right) \quad (13)$$

where l represents the thickness of PEM; ρ_m is the specific membrane resistance, which can be expressed as

$$\rho_m = \frac{181.6 \times \left[1 + 0.03 \times \left(\frac{i_{cell}}{A}\right) + 0.062 \times \left(\frac{T}{303}\right)^2 \left(\frac{i_{cell}}{A}\right)^{2.5}\right]}{\left[\lambda - 0.643 - 3 \times \left(\frac{i_{cell}}{A}\right)\right] \times \exp\left[4.18 \times \left(\frac{T-303}{T}\right)\right]} \quad (14)$$

where λ denotes the water content of PEM.

Besides, the concentration voltage loss V_{con} satisfy the following equations

$$V_{con} = -b \times \ln\left(1 - \frac{J}{J_{max}}\right) \quad (15)$$

$$J = \frac{i_{cell}}{A} \quad (16)$$

where b stands for the parameter coefficient; J and J_{max} denote the current density and the maximum current density, respectively.

2.3 Objective function

The purpose of parameter identification is to extract the unknown parameters to effectively minimize errors between the actual data and the calculated data. Similar to references [30-32], root mean square error (RMSE) is chosen as the objective function, as follows:

$$RMSE(x) = \sqrt{\frac{1}{N}\sum_{i=1}^{N}\left[V_{act}(i) - V_{cal}(i)\right]^2}, x = \left[\varepsilon_1, \varepsilon_2, \varepsilon_3, \varepsilon_4, \lambda, R_c, b\right] \quad (17)$$

where x represents unknown identified parameters; N is the number of *V-I* data sets; V_{act} and V_{cal} represent the actual operating voltage and calculated voltage.

3. FNN-POA for PEMFC parameter identification

3.1 Principle of FNN

A feedforward neural network (FNN) is an artificial neural network in which data information is transmitted from the front end to the back end without feedback. Its topological structure is shown in Fig. 3, which usually consists of an input layer, several hidden layers, and an output layer [30].

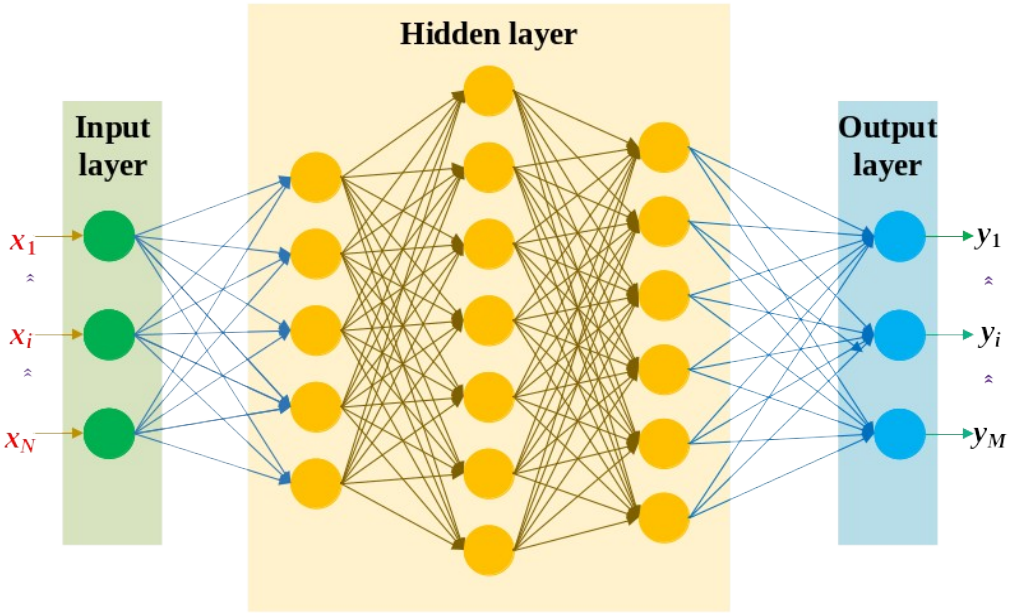

Fig. 3. Structure diagram of FNN.

The model of the nth neuron in the mth layer can be written as [33]

$$x_n^m = f\left(\sum_{i=1}^{T_{m-1}} w_{i,n}^m x_n^{m-1} + b_n^m\right) \tag{18}$$

where T_{m-1} is the neuron number in the (m-1)th layer; $w_{i,n}^m$ is the weight between the ith neuron in the (m-1)th layer and the nth neuron in the mth layer; b_n^m denotes the threshold value of the nth neuron in the mth layer; $f(\cdot)$ is the Sigmoid function, which is given as follows [34]:

$$f(x) = \frac{1}{1+e^{-x}} \tag{19}$$

where the mapping output of the Sigmoid function ranges from 0 to 1, and it owns so limited output range that a stable result can be obtained by optimizing the model.

This article adopts a hidden layer with 10 neurons. Additionally, Bayesian regularization is introduced as the model training function to improve the fitting accuracy and generalization ability of the network by modifying the weight of the network.

3.2 Pelican optimization algorithm

The optimization strategy is inspired by the hunting behavior of the pelican which mainly includes two phases: moving towards prey and winging on the water surface [35].

3.2.1 Initialization

During the initialization stage, the position of each population member is generated by

$$x_{i,j}=x_{min,j}+rand\times\left(x_{max,j}-x_{min,j}\right),i=1,2,\ldots,N,j=1,2,\ldots,D \quad (20)$$

where $x_{i,j}$ is the position of the ith pelican, namely the value of the jth variable in the ith candidate solution; N represents the number of the pelican population; D means the number of the dimensions of the problem; $rand$ denotes a random vector between 0 and 1; $x_{min,j}$ and $x_{max,j}$ is the jth lower bound and upper bound, respectively.

3.2.2 Moving Towards Prey

During the pelican's pursuit phase, the first step is to locate the prey and move toward the identified zone, which can be expressed as [35]

$$x_{i,j}^{M}=\begin{cases}x_{i,j}+rand\times\left(p_j-I\times x_{i,j}\right), if\ F_p<F_i\\ x_{i,j}+rand\times\left(x_{i,j}-p_j\right), otherwise\end{cases} \quad (21)$$

where $x_{i,j}^{M}$ denotes the new position of the ith pelican in the jth dimension under pursuit phase; I represents a random number which is equal to 1 or 2; p_j is the position of the jth prey; F_p is the best objective function value of the *i*-1 pelican; F_i stands for the objective function value of the ith pelican. Note that the pelican will generate more displacement to enhance exploration when I is equal to 2. To prevent pelicans from moving to suboptimal areas, Eq. (22) is designed as follows:

$$X_i=\begin{cases}X_i^{M}, if\ F_i^{M}<F_i\\ X_i, otherwise\end{cases} \quad (22)$$

where X_i^{M} and F_i^{M} represent the new position and objective function value of the ith pelican, respectively.

3) Winging on the water surface

During the pelican's attack phase, they will reach the water surface and then spread their wings to move the prey upwards. This strategy leads pelicans can catch more prey in the attack area, which can be described as [36]

$$x_{i,j}^{W}=x_{i,j}+0.2\times\left(1-\frac{t}{T}\right)\times\left(2\times rand-1\right)\times x_{i,j} \quad (23)$$

where $x_{i,j}^{W}$ denotes the new position of the ith pelican in the jth dimension based on the attack phase; $0.2\times\left(1-\frac{t}{T}\right)$ represents the neighborhood radius of $x_{i,j}$, where t and T are current iterations and maximum iterations, individually. Through hunting nearby local areas, the searchability of POA can be significantly improved. Also, the same method as Eq. (22) is used

to limit the displacement.

3.3 The parameter identification process of FNN-POA

The PEMFC parameter identification process of FNN-POA can be roughly divided into three parts: data collection, data preprocessing, and parameter identification, as depicted in Fig. 4.

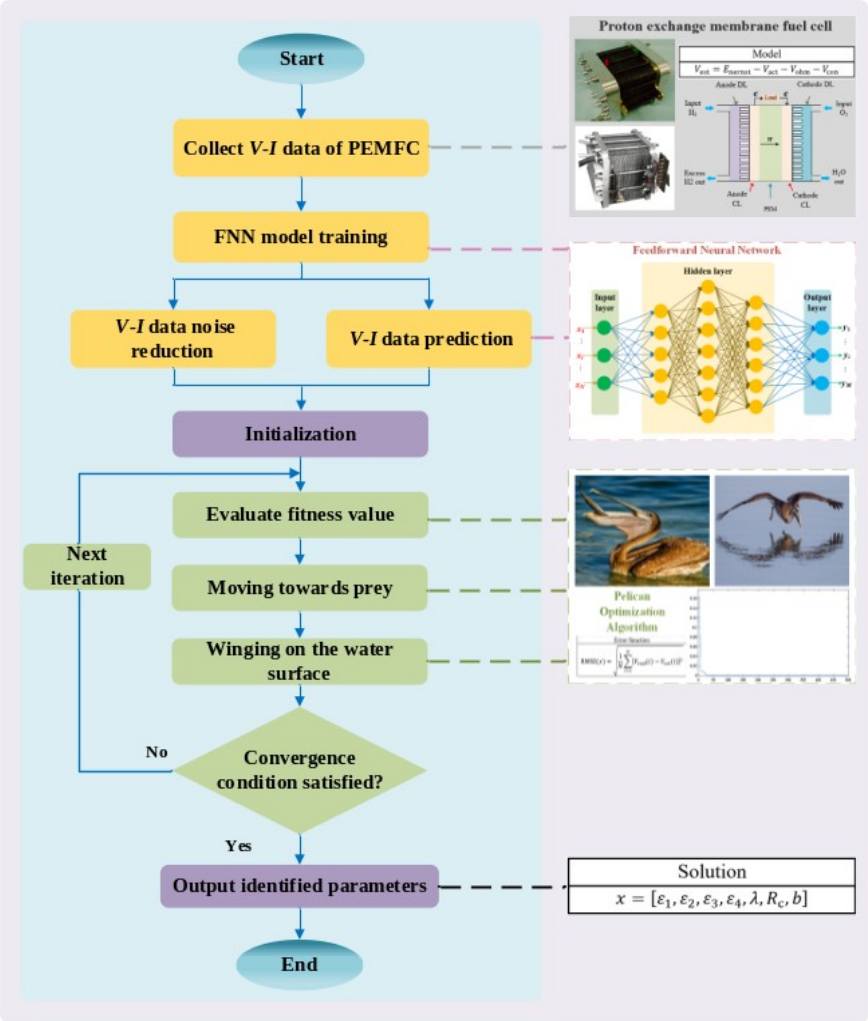

Fig. 4. The flow chart of the FNN-POA.

The concrete process can be summarized as follows: Firstly, actual *V-I* data of PEMFC are collected to train the FNN model; Then the trained model is adopted to denoise and predict data; Finally, POA is used to optimize the unknown parameters of the PEMFC model via iterations.

4. Case studies

The temperature and relative humidity of vapor at the anode and cathode have a strong influence on the parameter identification. Subsequently, MhAs are employed to extract the parameters of the PEMFC model under three operating conditions, tabularized in Table 2.

These MhAs include multi-verse optimizer (MVO) [21], improved whale optimization algorithm (IWOA) [37], grey wolf optimization (GWO) [38], Harris hawk optimization (HHO) [39], artificial jellyfish search (JS) [20], moth-flame optimization (MFO) [40], pelican optimization algorithm (POA) [35], and teaching-learning-based optimization (TLBO) [41].

Table 2. Three operating conditions of PEMFC.

Operation conditions	T_k(K)	Rh_a(atm)	Rh_c(atm)
HTLP	353.15	1	1
MTMP	333.15	2	2
LTHP	313.15	3	3

In addition, the parameter range of Ballard-Mark-V PEMFC with a film thickness of 178 μm^2 and effective area of 50.6 cm^2 are provided in Table 3, which are gathered from reference [43].

Table 3. PEMFC parameter range for identification

Model parameters	ε_1	ε_2	ε_3	ε_4	λ	R_c(Ω)	b(V)
Minimum	-1.1997	0.0010	3.6000E-05	-2.6000E-04	10.0000	1.0000E-04	0.0136
Maximum	-0.8531	0.0050	9.8000E-05	-9.5400E-04	23.0000	8.0000E-04	0.5000

Considering the noise interference and limited available data, 25 pairs of current-voltage data extracted from the cell are regarded as original data. For the sake of impartial comparison, the maximum iteration number of each algorithm is equally set to 500 times. Meanwhile, 10 times independent operations are executed to evaluate the stability of MhAs.

4.1 Preprocessing of neural network

The measurement error of the monitoring instrument and the interference of the operating condition has a great influence on the data collection work. Therefore, this paper proposes to use a neural network to preprocess the collected data. These neural networks include back propagation (BP) neural network, long short term memory (LSTM) neural network, general regression neural network (GRNN), and feedforward neural network (FNN).

Figure 5 gives the noise data and denoised data obtained by each neural network under three operating conditions. The correlation coefficient R^2 between ideal data and denoised data is introduced to quantify the noise reduction effect. The denoised data obtained by FNN can well match the ideal data. Moreover, FNN can always acquire the largest R^2 compared with other methods, i.e., 99.98%, 99.99%, and 99.64% under HTLP, MTMP, and LTHP, respectively. Therefore, FNN is recommended as the best candidate for efficient noise reduction.

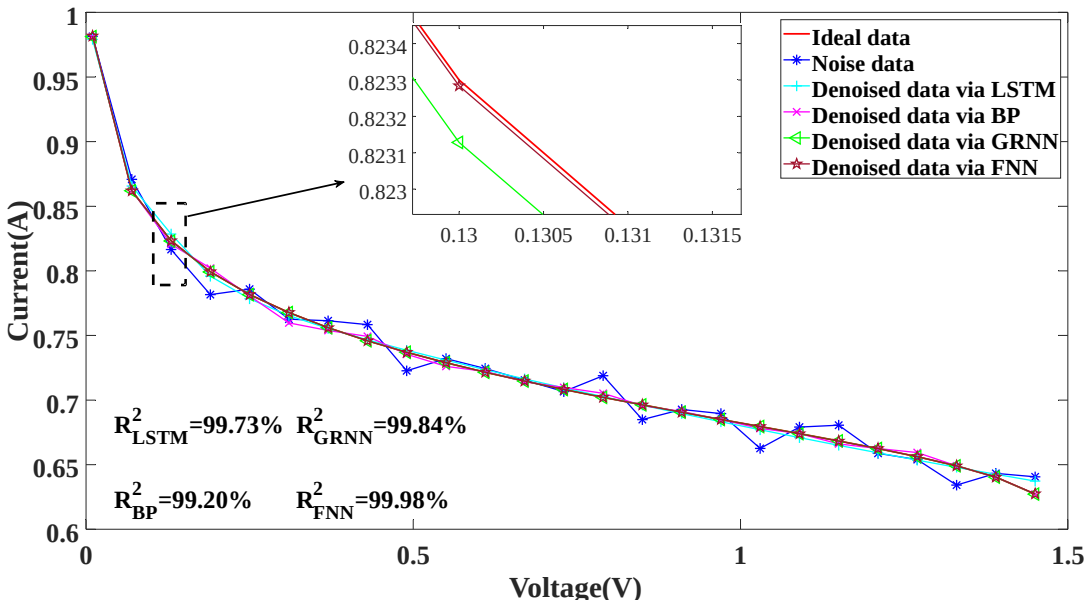
Ideal data
Noise data
Denoised data via LSTM
Denoised data via BP
Denoised data via GRNN
Denoised data via FNN
Current(A)
Voltage(V)
R^2_{LSTM}=99.73% R^2_{GRNN}=99.84%
R^2_{BP}=99.20% R^2_{FNN}=99.98%

(a)

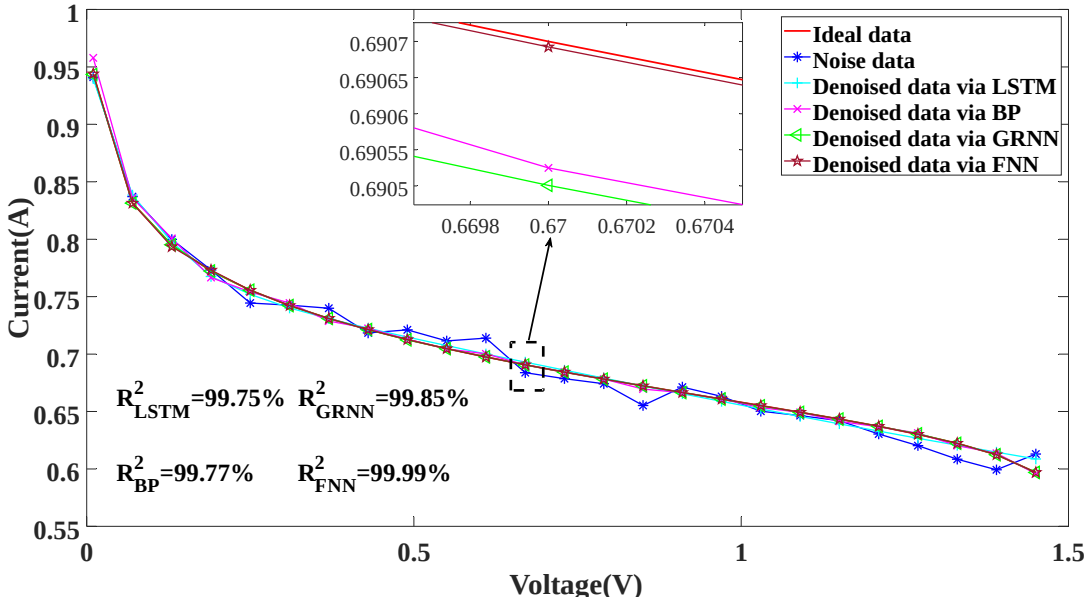
Ideal data
Noise data
Denoised data via LSTM
Denoised data via BP
Denoised data via GRNN
Denoised data via FNN
Current(A)
Voltage(V)
R^2_{LSTM}=99.75% R^2_{GRNN}=99.85%
R^2_{BP}=99.77% R^2_{FNN}=99.99%

(b)

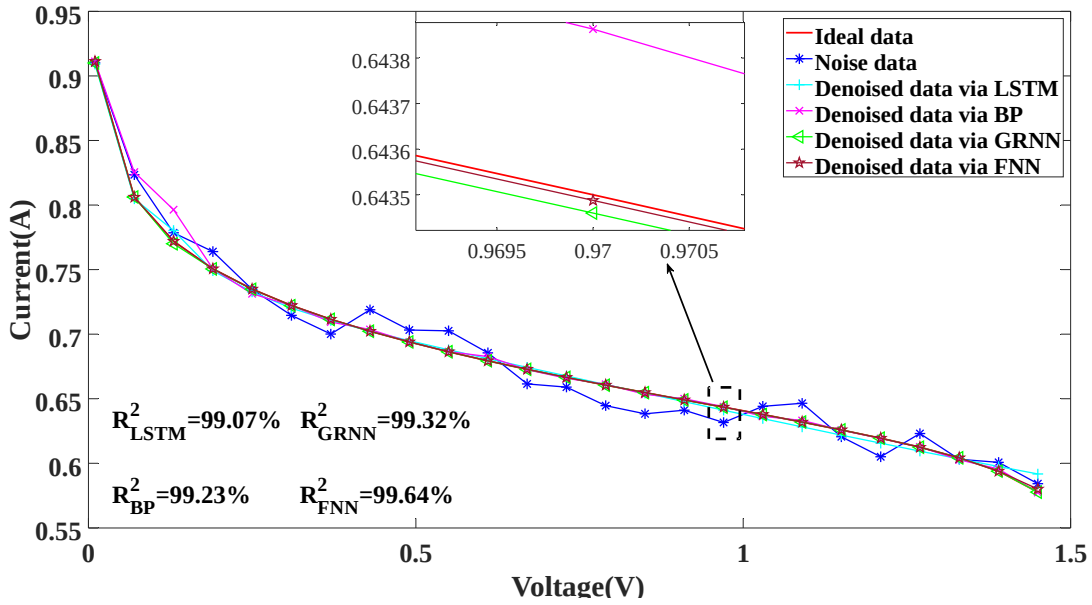

(c)

Fig. 5. Noise reduction results under three operating conditions via different neural networks: (a) HTLP; (b) MTMP; and (c) LTHP.

Moreover, data prediction results under three operating conditions via various neural networks are shown in Figure 6. The predicted curves acquired by BP and GRNN fluctuate around the ideal data curve. Also, the curve of LSTM has the maximum deviation from the ideal data curve. Inspiringly, the predicted curve obtained by FNN is closest to the ideal data curve.

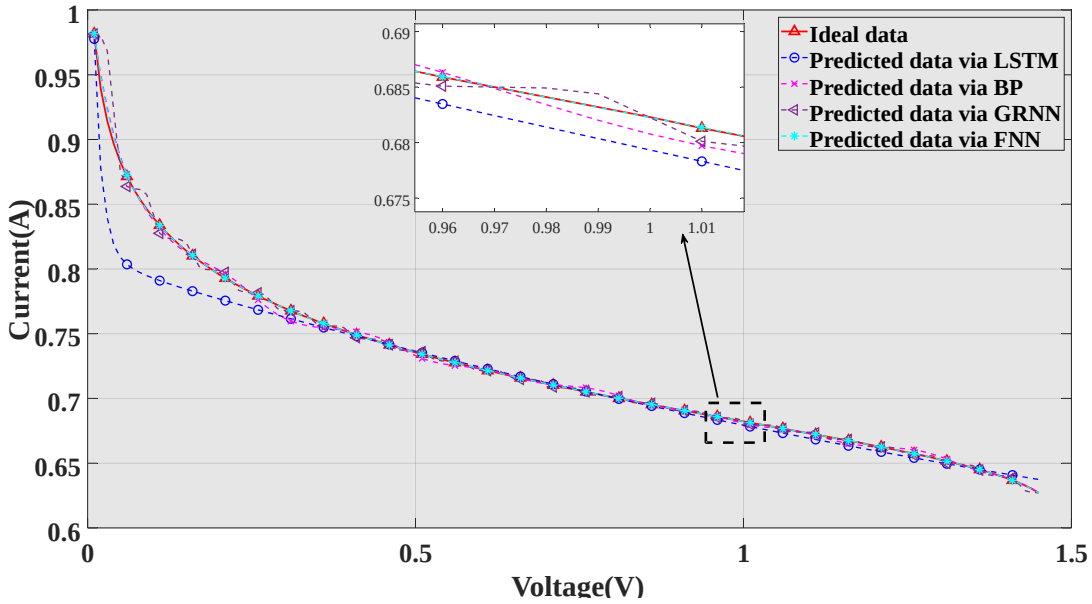

(a)

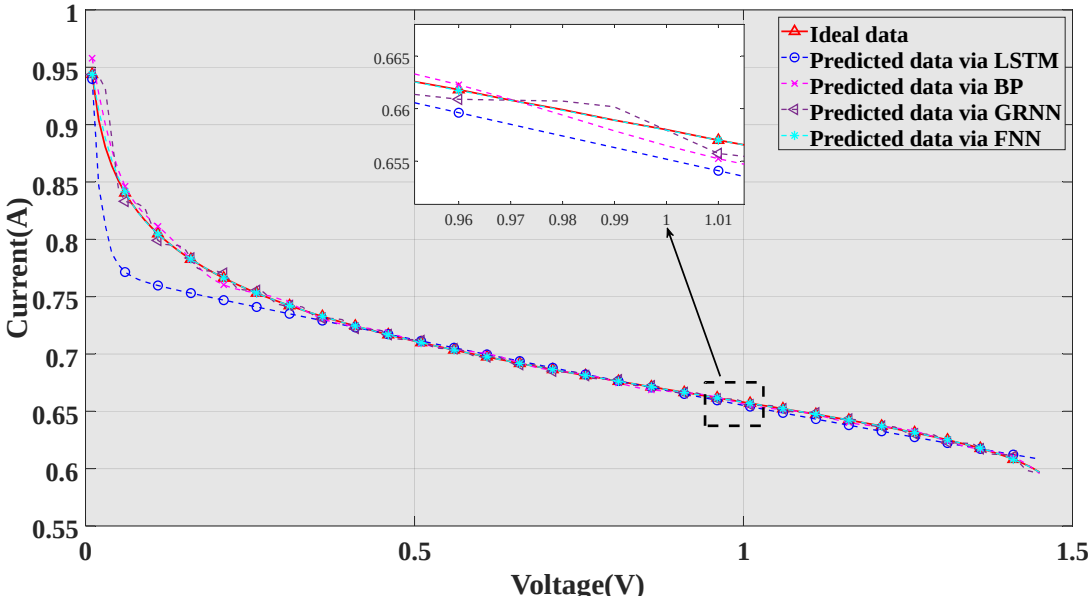

(b)

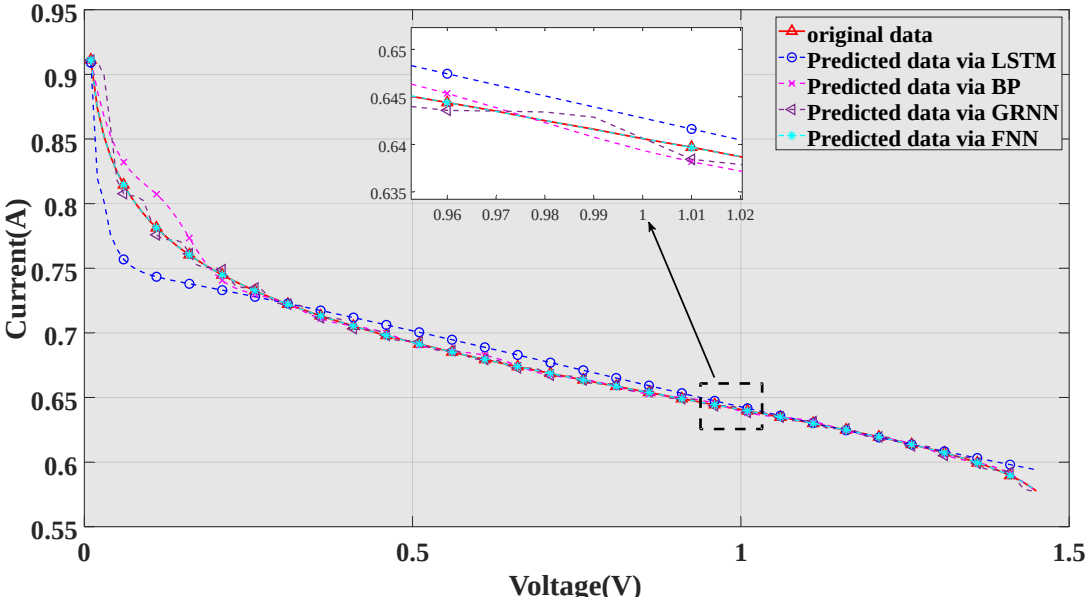

(c)

Fig. 6. Date prediction results under three operating conditions via different neural networks: (a) HTLP; (b) MTMP; and (c) LTHP.

4.2 The preprocessing of *V-I* data by FNN

4.2.1 The noise reduction of *V-I* data by FNN

Two types of noise data (i.e., Gaussian white noise and Rayleigh white noise) are introduced to possibly simulate the disturbances from various factors (e.g., data collecting instrument and complex operating conditions) and to verify the effectiveness of FNN in noise reduction. Figure 7 offers the noise reduction results of FNN under three different Gaussian white noise with a signal-to-noise ratio (SNR) of 20 dB, 25 dB, and 35 dB. It is easy to see denoised data obtained by FNN can better match the ideal data curve, which means FNN has

an outstanding performance for noise reduction.

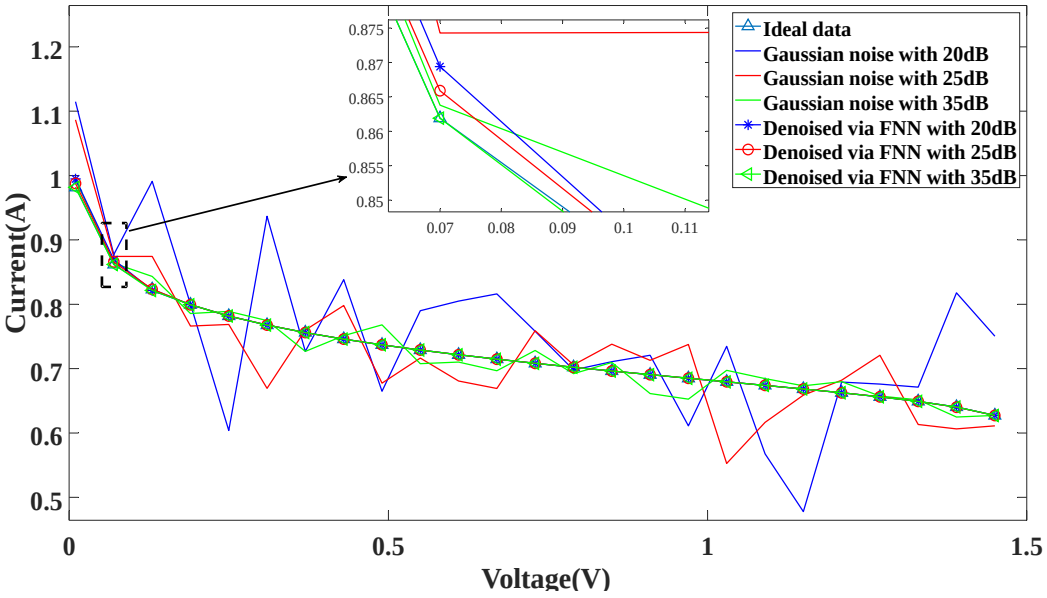

(a)

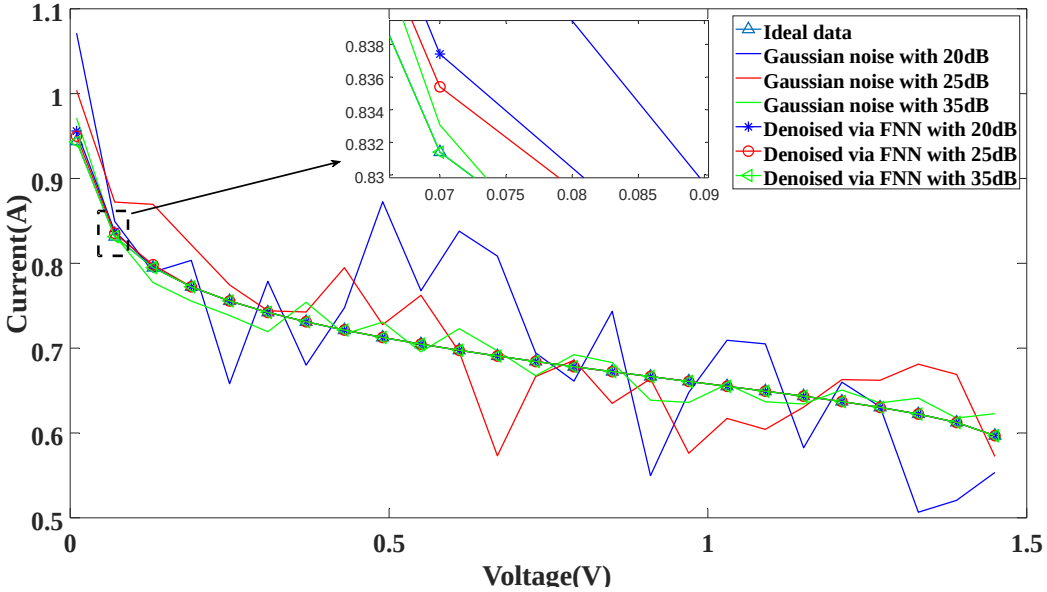

(b)

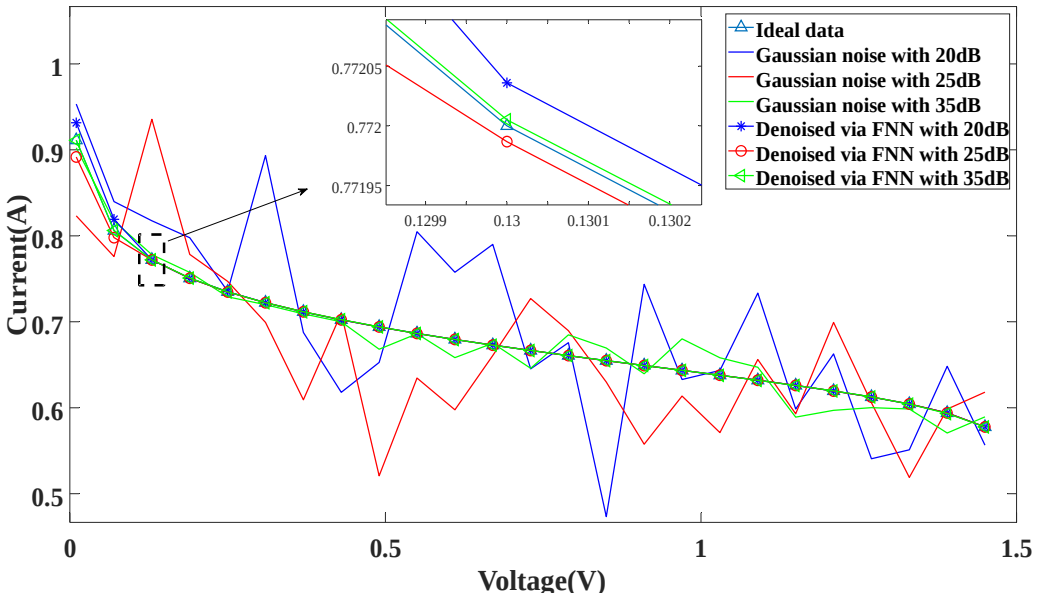

(c)

Fig. 7. Gaussian noise reduction results under three operating conditions: (a)HTLP; (b) MTMP; and (c) LTHP.

In addition, Rayleigh white noise is employed to further evaluate the denoised performance of FNN. As shown in Fig. 8, with the increase of SNR, more ideal denoised data can be acquired. To simplify the validation work, 35 dB white Gaussian noise data is used in the following parameter identification.

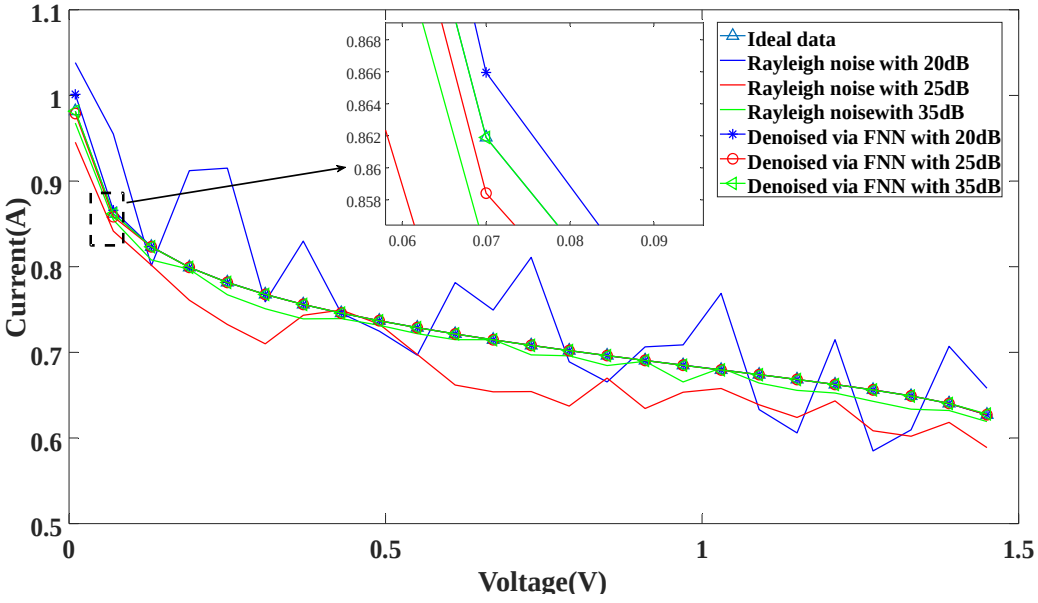

(a)

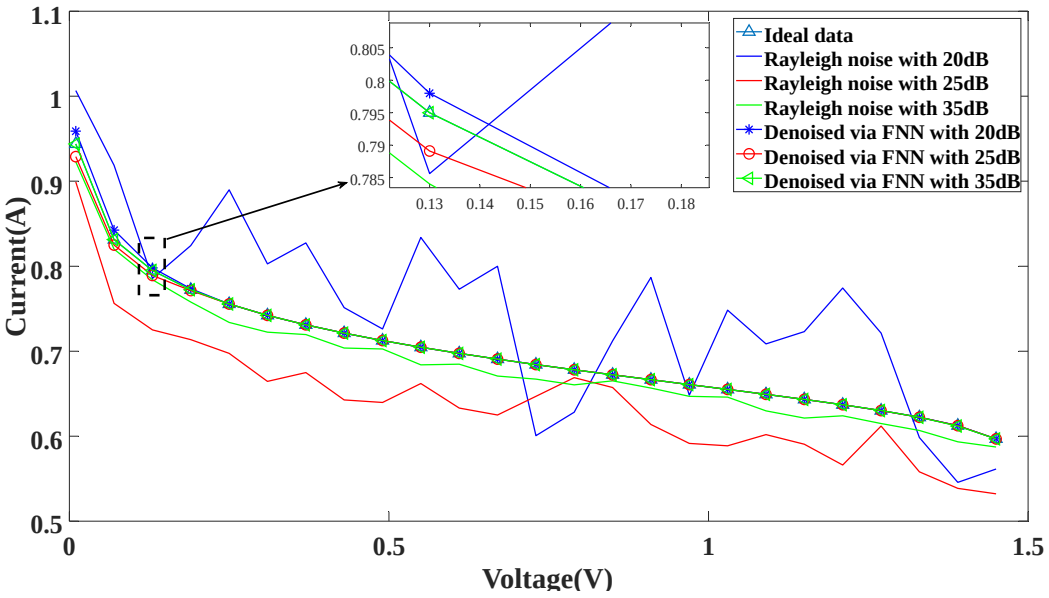

(b)

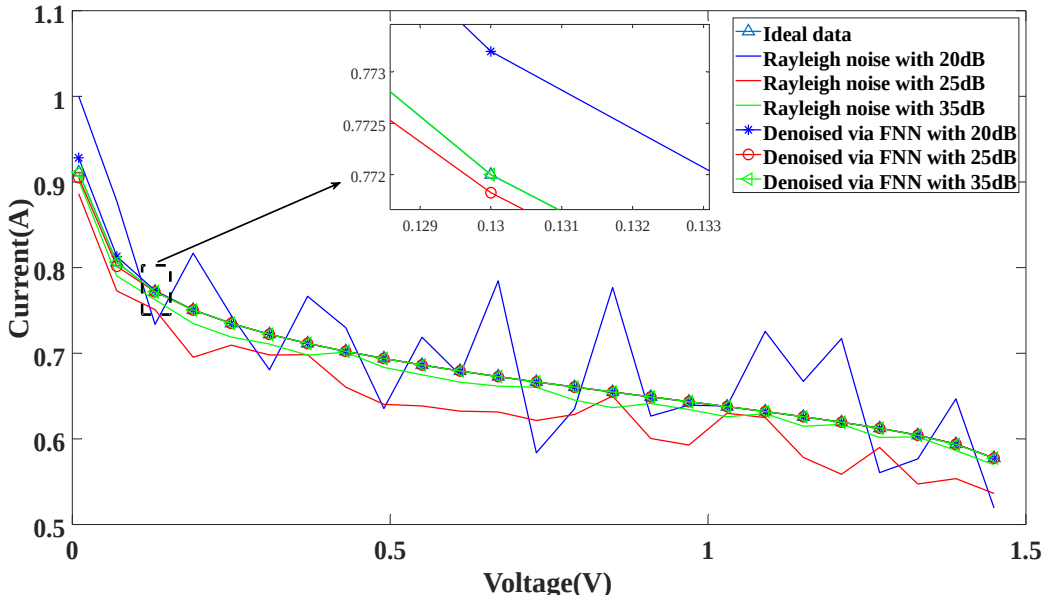

(c)

Fig. 8. Rayleigh noise reduction results under three operating conditions: (a)HTLP; (b) MTMP; and (c) LTHP.

4.2.2 The prediction of *V-I* data by FNN

The results of data prediction obtained by FNN are shown in Fig. 9, upon which 120 sets of high-quality predicted data can be obtained. One can easily observe that FNN predicts results that are very close to the ideal data through the fast oscillation approach, which expresses the excellent data prediction capability of FNN.

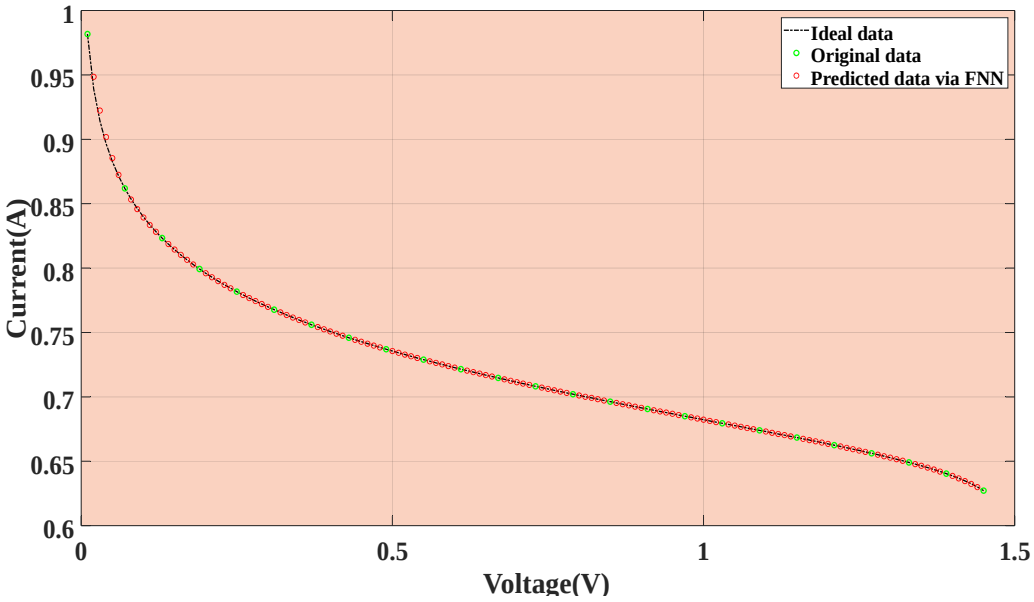
Ideal data
Original data
Predicted data via FNN
Current(A)
Voltage(V)
1
0.95
0.9
0.85
0.8
0.75
0.7
0.65
0.6
0
0.5
1
1.5

(a)

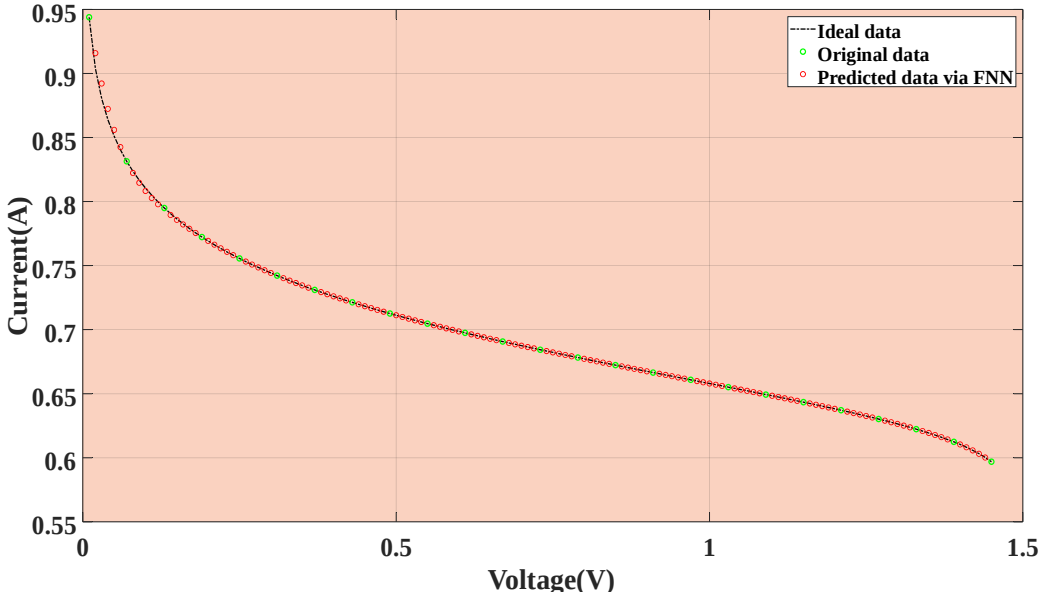
Ideal data
Original data
Predicted data via FNN
Current(A)
Voltage(V)
0.95
0.9
0.85
0.8
0.75
0.7
0.65
0.6
0.55
0
0.5
1
1.5

(b)

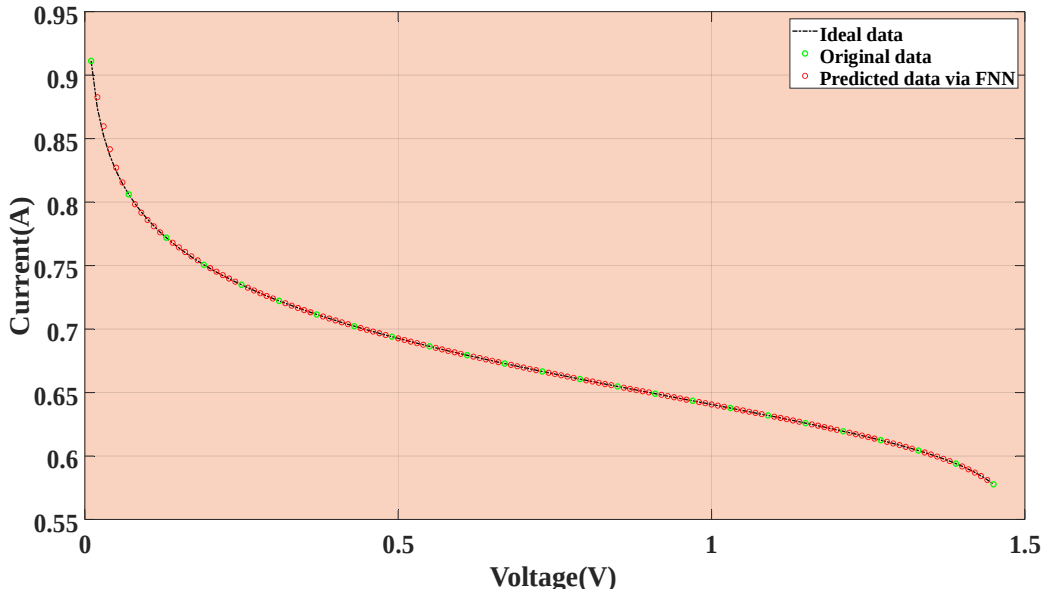

(c)

Fig. 9. Date prediction results under three operating conditions: (a)HTLP; (b) MTMP; and (c) LTHP.

4.3 PEMFC parameter identification of HTLP

4.3.1 Noise reduction data

The parameter identification results of MhAs for noised data and denoised data under HTLP are tabulated in Table 4, where the symbol 'N' expresses the identification results obtained by noised data and the symbol 'DN' means those obtained by denoised data. From Table 4, it can be seen that RMSE from denoised data is smaller than that from noised data. In particular, POA exhibits the best performance and has the most significant RMSE decrease of 96.46%, whereas IWOA has a comparatively minimum reduction of 39.37%. Although RMSE from denoised and noise data of JS, POA enjoys a more pronounced drop.

Table 4. Parameter identification results of noised data and denoised data under MhAs.

State	Algorithms	Data	Identified parameters							RMSE
			ε_1	ε_2	ε_3	ε_4	λ	$R_c(\Omega)$	b(V)	
HTLP	MVO	N	-1.1518	3.8681E-03	8.2200E-05	-1.7265E-04	23.0000	1.9485E-04	0.0152	6.4417E-03
		DN	-0.8735	2.9398E-03	7.3804E-05	-1.7322E-04	21.5945	5.5895E-04	0.0136	3.1529E-04
	IWOA	N	-0.8531	3.2130E-03	9.5500E-05	-1.5908E-04	14.9181	7.8145E-04	0.0236	1.0827E-02
		DN	-0.8531	2.3220E-03	3.6000E-05	-1.6832E-04	10.0000	1.0373E-04	0.0136	6.5931E-03
	GWO	N	-0.9471	2.8987E-03	5.5600E-05	-1.7235E-04	14.6009	4.2108E-04	0.0144	6.3926E-03
		DN	-0.9465	3.1977E-03	7.7322E-05	-1.7318E-04	21.8454	4.0814E-04	0.0136	2.7858E-04
	HHO	N	-1.1980	3.7267E-03	6.3600E-05	-1.7163E-04	10.9784	7.1836E-04	0.0137	6.3408E-02
		DN	-1.1988	3.3091E-03	3.6090E-05	-1.5634E-04	10.0249	3.6544E-04	0.0264	3.0542E-03
	JS	N	-1.0383	3.4575E-03	7.6000E-05	-1.7228E-04	11.7147	4.0890E-04	0.0138	6.3611E-03
		DN	-1.0396	3.3115E-03	6.7036E-05	-1.7352E-04	22.9021	4.2615E-04	0.0136	2.8624E-04
	MFO	N	-1.1755	3.2579E-03	3.6000E-05	-1.7245E-04	23.0000	8.0000E-04	0.0150	6.4326E-03
		DN	-1.0588	3.8192E-03	9.8000E-05	-1.7309E-04	23.0000	8.0000E-04	0.0136	3.1222E-04

TLBO	N	-0.8532	3.3978E-03	9.8000E-05	-1.9301E-04	13.3947	1.0000E-04	0.0136	6.3311E-03
	DN	-0.9862	3.3543E-03	6.6186E-05	-1.9480E-04	23.0000	1.0000E-04	0.0136	5.6032E-04
POA	N	-1.0015	3.5294E-03	8.8100E-05	-1.7182E-04	10.8469	2.4698E-04	0.0136	6.3375E-03
	DN	-1.1943	3.3659E-03	4.0913E-05	-1.7342E-04	23.0000	3.9860E-04	0.0136	2.2430E-04

In addition, Figure 10 provides convergence curves of eight algorithms under noised data and denoised data, which indicates that RMSE obtained by denoised data is smaller than that obtained by noised data. Particularly, POA can not only quickly find the global optimal solution, but also has a relatively excellent optimization ability. Based on denoised data, POA acquires the smallest RMSE while IWOA, TLBO, and MFO prematurely converge to local optimum which demonstrates POA has a superior global searching ability. Meanwhile, MVO, GWO, JS, MFO, TLBO, and POA represent the same accuracy of convergence results based on noise data, but POA shows an apparent dominance of identified results based on denoised data.

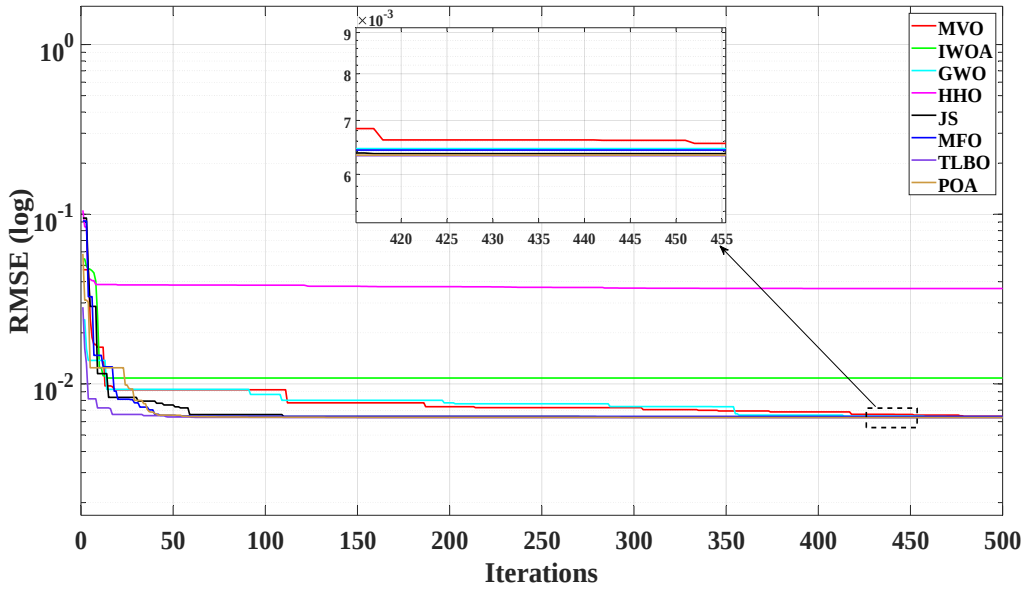

(a)

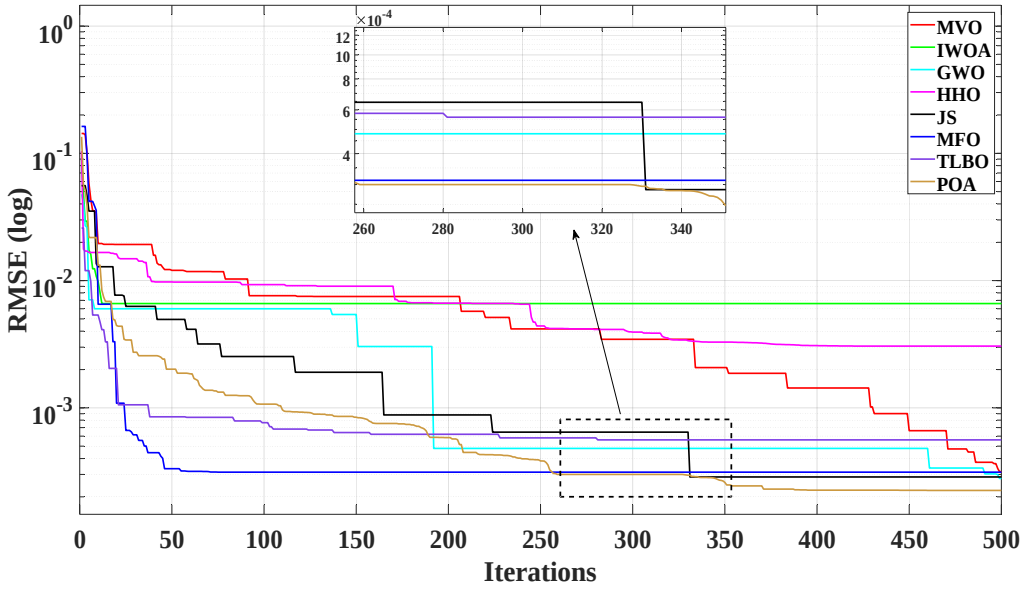

(b)

Fig. 10. Convergence curves of RMSE obtained by MhAs under HTLP: (a) noised data and (b) denoised data.

Boxplot of eight algorithms is shown in Fig. 11, which illustrates that RMSE obtained by denoised data has a smaller distribution range and upper/lower bounds compared with the RMSE obtained by noised data. Compared with MOA, IWOA, GWO, and HHO, POA can acquire the smaller bound boxplot, which demonstrates the excellent performance of POA for parameter identification in terms of high accuracy and reliable stability.

Besides, the statistical results of the minimum, median, mean, maximum, and standard deviation (SD) of RMSE are listed in Table 5, where POA can obtain the majority of satisfactory results except the SD. Therefore, it can be summarized that POA owns the most satisfactory performance under HTLP.

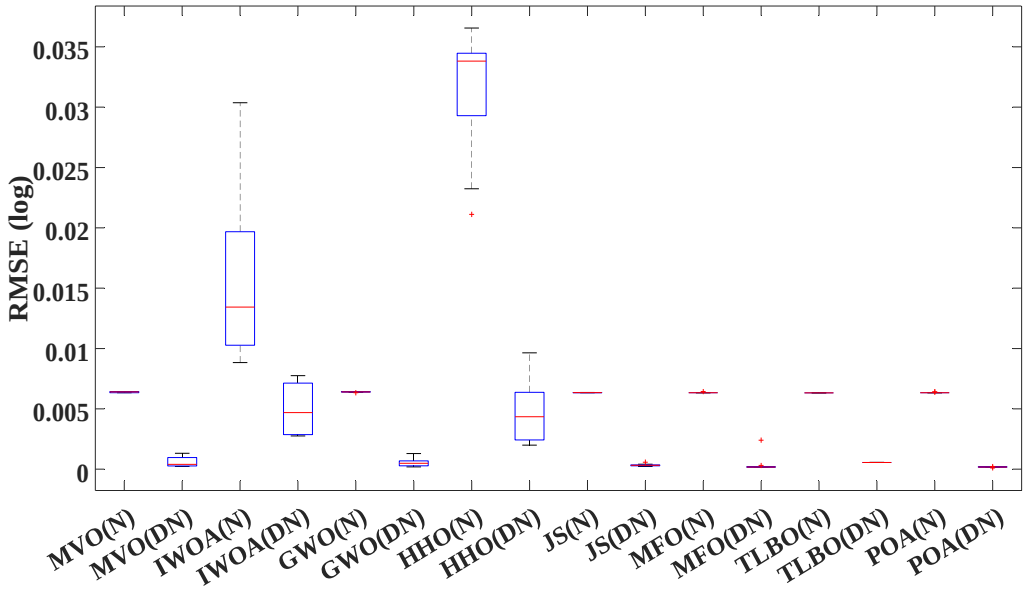

Fig. 11. Boxplot of RMSE obtained by MhAs under HTLP.

Table 5. Statistical results of RMSE obtained by denoised data.

Algorithm	RMSE				
	Min.	Median	Mean	Max.	SD
MVO	1.4629E-04	5.9580E-04	5.4739E-04	1.2668E-03	3.3654E-04
IWOA	1.4032E-03	2.0762E-03	2.5393E-03	4.4876E-03	1.0972E-03
GWO	1.6185E-04	2.2832E-04	2.4727E-04	4.1777E-04	8.1323E-05
HHO	2.1208E-03	1.8809E-02	1.5712E-02	2.2568E-02	7.5213E-03
JS	1.3848E-04	2.1004E-04	2.4292E-04	4.0757E-04	8.6959E-05
MFO	1.2979E-04	1.4479E-04	1.4870E-04	1.8156E-04	1.8069E-05
TLBO	3.6076E-04	3.6398E-04	3.7422E-04	4.4415E-04	2.5432E-05
POA	1.1695E-04	1.4260E-04	1.4918E-04	1.7915E-04	2.1806E-05

Figure 12 presents the *V-I* characteristic curve of POA with the best performance based on the denoised data under HTLP. It can be seen that the curve of fitting data highly overlaps with that of actual data. Moreover, the RMSE is equal to 99.51% between 25 sets of *V-I* data inversely derived from the identification results and the measured data.

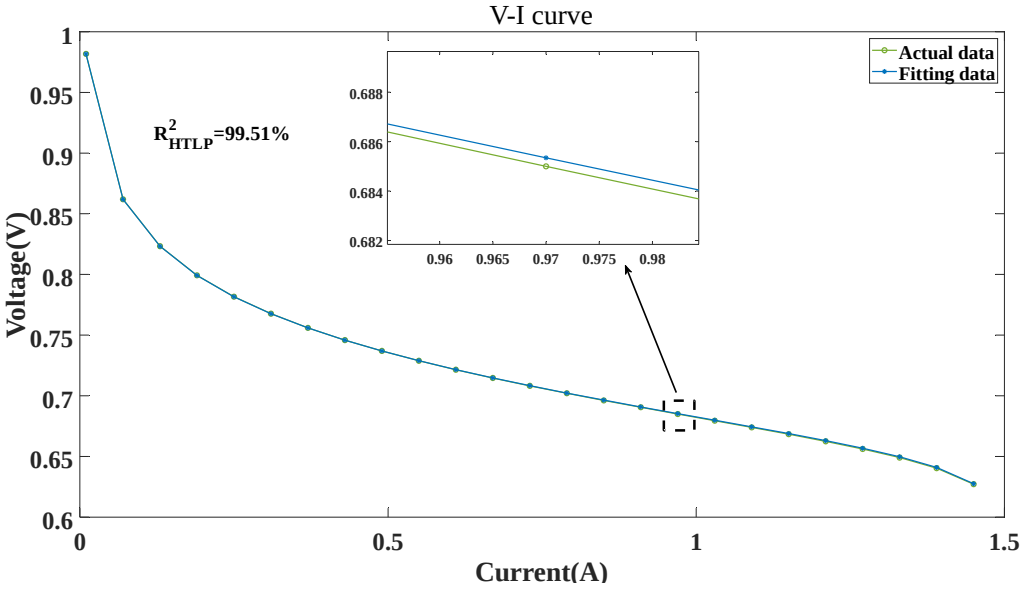

Fig. 12. FNN for *V-I* curve fitting based on denoised data under HTLP of POA.

4.3.2 Predicted data

The parameter identification results of MhAs for original data and predicted data under HTLP are tabulated in Table 6, where the symbol 'O' and 'P' stand for original data and predicted data, respectively. Compared with RMSE obtained by original data, that from predicted data is smaller i.e. POA has a clear reduction of 41.79%. Especially, based on predicted data, POA has the smallest RMSE, followed by MFO, MVO, JS, GWO, TLBO, IWOA, and HHO.

Table 6. Parameter identification results of original data and predicted data under MhAs.

State	Algorithms	Data	Identified parameters							RMSE
			ε_1	ε_2	ε_3	ε_4	λ	$R_c(\Omega)$	b(V)	
HTLP	MVO	O	-1.0831	3.5503E-03	7.4969E-05	-1.7279E-04	19.2388	7.8495E-04	0.0136	4.9210E-04
		P	-1.1941	4.1172E-03	9.2184E-05	-1.7331E-04	22.7382	7.4105E-04	0.0136	1.8705E-04

IWOA	O	-0.8531	2.4405E-03	4.6125E-05	-1.5459E-04	13.0083	3.8121E-04	0.0200	9.7089E-03
	P	-0.9703	2.7916E-03	4.6067E-05	-1.6611E-04	10.0000	2.1106E-04	0.0136	2.0844E-03
GWO	O	-1.0501	3.4598E-03	7.5202E-05	-1.7163E-04	13.5401	7.3495E-04	0.0137	1.2369E-03
	P	-0.9200	2.8262E-03	5.7114E-05	-1.7294E-04	20.0027	6.0503E-04	0.0136	2.5299E-04
HHO	O	-0.9138	2.4130E-03	3.6019E-05	-1.1628E-04	10.0053	2.9938E-04	0.0351	2.8708E-02
	P	-1.0210	3.0240E-03	4.9799E-05	-1.7801E-04	13.7873	3.5080E-04	0.0136	2.5786E-03
JS	O	-0.9685	2.9743E-03	5.7749E-05	-1.7347E-04	20.7190	2.5012E-04	0.0137	4.1723E-04
	P	-0.9456	3.2006E-03	7.7645E-05	-1.7340E-04	21.9637	3.2823E-04	0.0136	2.2402E-04
MFO	O	-0.9495	2.6005E-03	3.6000E-05	-1.7361E-04	23.0000	1.0000E-04	0.0136	1.8172E-04
	P	-1.1997	3.5086E-03	4.9576E-05	-1.7362E-04	22.2940	1.0000E-04	0.0136	1.3652E-04
TLBO	O	-0.8531	2.5236E-03	3.8050E-05	-1.9472E-04	23.0000	1.0000E-04	0.0136	5.5224E-04
	P	-1.0237	3.1636E-03	4.4423E-05	-1.9459E-04	23.0000	1.0077E-04	0.0136	3.6277E-04
POA	O	-1.1598	4.1051E-03	9.8000E-05	-1.7342E-04	22.4447	2.3202E-04	0.016	2.2296E-04
	P	-0.9643	2.6431E-03	3.6005E-05	-1.7362E-04	23.0000	3.3128E-04	0.0136	1.2979E-04

In addition, Figure 13 provides a convergence curves graph of MhAs under original data and predicted data, which indicates that RMSE is decreased after using predicted data to identify parameters. Furthermore, MFO and POA are the two best algorithms. Under the original data case, MFO can rapidly find the globally optimal solution to diminish RMSE, followed by POA. Under predicted data, POA converges to the smallest RMSE with the fastest speed.

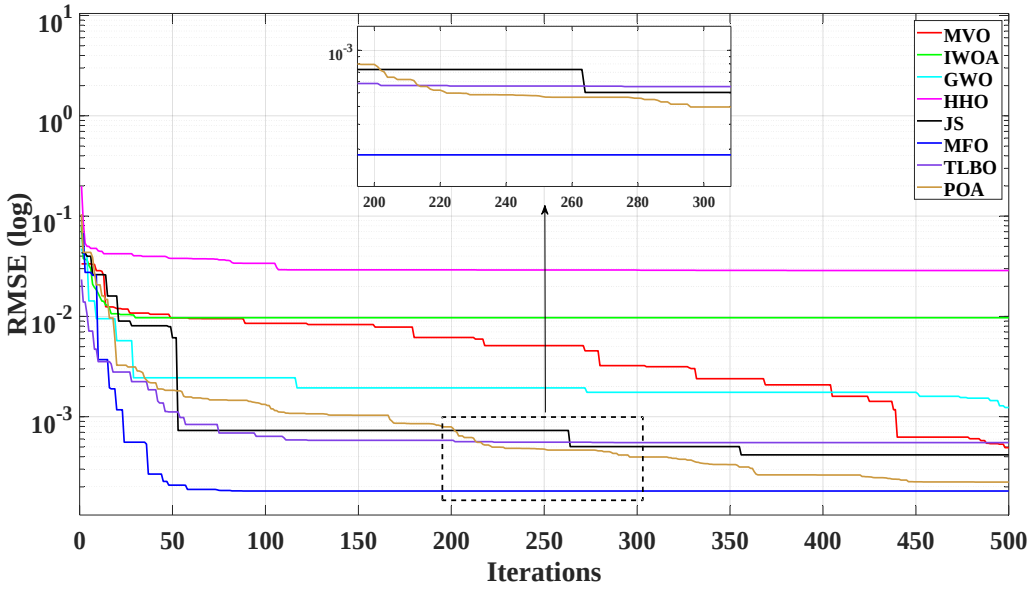

(a)

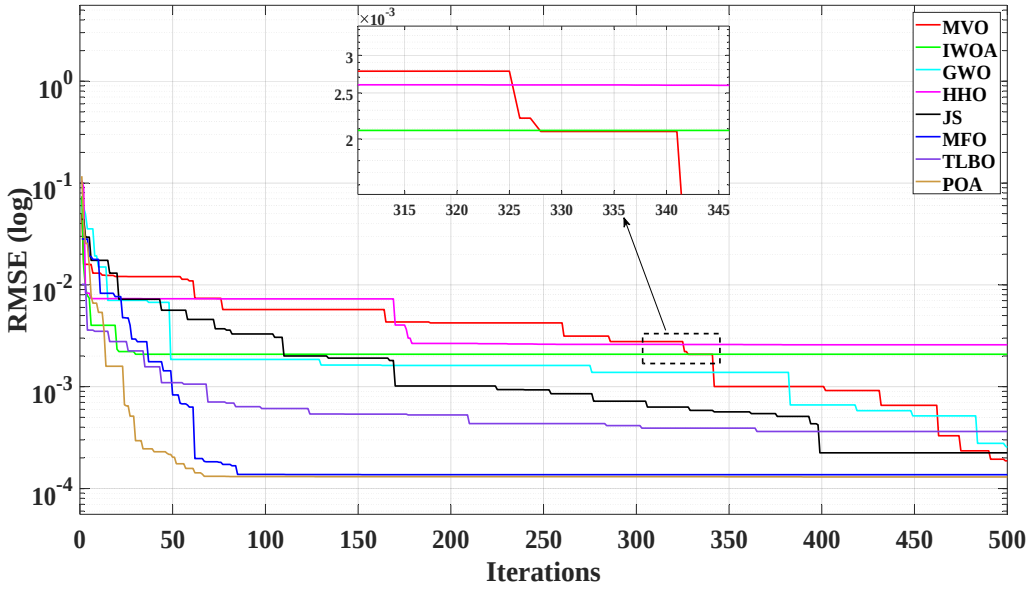

(b)

Fig. 13. Convergence curves of RMSE obtained by MhAs under HTLP: (a) original data and (b) predicted data.

Boxplot of eight algorithms in 10 separate runs is depicted in Fig. 14, which illustrates that RMSE based on predicted data has a smaller distribution range and upper/lower bounds compared with that based on original data. Compared with constant algorithms, the predicted data based on a boxplot of POA enjoys the smallest distribution range and lowest upper/lower bounds, which means POA can search for the most suitable parameters with the highest stability.

Furthermore, the statistical results of RMSE are listed in Table 7, where POA can obtain the majority of satisfactory results while only the SD of MFO is better than that of POA. Therefore, it can be simply summarized that POA owns the best consistent performance under HTLP.

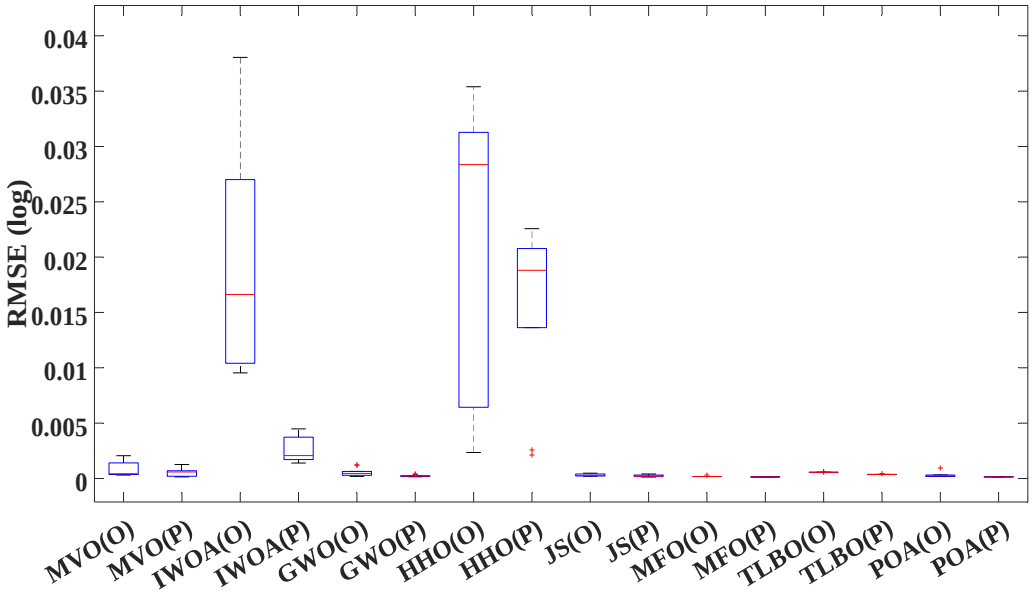

Fig. 14. Boxplot of RMSE obtained by MhAs under HTLP.

Table 7. Statistical results of RMSE obtained by predicted data.

Algorithm	RMSE				
	Min.	Median	Mean	Max.	SD
MVO	1.4629E-04	5.9580E-04	5.4739E-04	1.2668E-03	3.3654E-04
IWOA	1.4032E-03	2.0762E-03	2.5393E-03	4.4876E-03	1.0972E-03
GWO	1.6185E-04	2.2832E-04	2.4727E-04	4.1777E-04	8.1323E-05
HHO	2.1208E-03	1.8809E-02	1.5712E-02	2.2568E-02	7.5213E-03
JS	1.3848E-04	2.1004E-04	2.4292E-04	4.0757E-04	8.6959E-05
MFO	1.3652E-04	1.4479E-04	1.5072E-04	1.8156E-04	1.5879E-05
TLBO	3.6076E-04	3.6398E-04	3.7422E-04	4.4415E-04	2.5432E-05
POA	1.2979E-04	1.4260E-04	1.5046E-04	1.7915E-04	1.9997E-05

4.4 PEMFC parameter identification of MTMP

4.4.1 Noise reduction data

The parameter identification results of MhAs for noised data and denoised data are tabulated in Table 8. Here, it can be seen that, compared with RMSE obtained from noised data, RMSE from denoised data is better. Particularly, POA exhibits the best performance and has the most significant decrease of 99.84%, whereas GWO has a comparatively minimum reduction of 78.91%. Moreover, under denoised data, the RMSE of the POA has a magnitude of the minus six power of ten, while the RMSE of the best of other algorithms has a magnitude of the minus five power of ten.

Table 8. Parameter identification results of noised data and denoised data under MhAs.

State	Algorithms	Data	Identified parameters							RMSE
			ε_1	ε_2	ε_3	ε_4	λ	$R_c(\Omega)$	b(V)	
MTMP	MVO	N	-1.0009	3.1951E-03	6.8057E-05	-1.6655E-04	21.3934	4.7426E-04	0.0136	6.0683E-03
		DN	-0.9414	2.7758E-03	4.9912E-05	-17426E-04	12.8113	7.7709E-04	0.0149	1.6005E-04
	IWOA	N	-0.9298	2.4782E-03	4.0925E-05	-1.0943E-04	16.1227	1.0894E-04	0.0300	2.9663E-02
		DN	-0.8531	2.3269E-03	3.7900E-05	-1.7119E-04	11.8382	6.0437E-04	0.0136	2.3003E-03
	GWO	N	-0.9065	3.2239E-03	8.9583E-05	-1.6675E-04	19.4878	1.4998E-04	0.0136	6.1142E-03
		DN	-0.9724	3.0573E-03	6.2952E-05	-1.7264E-04	18.0840	1.0141E-04	0.0162	1.2895E-03
	HHO	N	-0.9986	2.6184E-03	3.6000E-05	-1.1103E-04	10.0000	1.0000E-04	0.0258	2.8590E-02
		DN	-1.0826	3.4979E-03	6.9440E-05	-1.7171E-04	15.8584	5.3949E-04	0.0208	5.9204E-03
	JS	N	-1.1055	3.3898E-03	5.9891E-05	-1.6678E-04	22.6664	1.197E-04	0.0136	5.9367E-03
		DN	-0.9480	3.1032E-03	7.1206E-05	-1.7218E-04	14.6758	5.4998E-04	0.0155	4.5147E-05
	MFO	N	-1.1997	4.2245E-03	9.8000E-05	-1.6694E-04	23.0000	1.0000E-04	0.0136	5.9095E-03
		DN	-1.1699	3.4826E-03	5.1354E-05	-1.7205E-04	10.0000	1.0000E-04	0.0136	2.8249E-04
	TLBO	N	-0.8531	2.2887E-03	3.6004E-05	-1.6700E-04	23.0000	1.0012E-04	0.0136	5.8950E-03
		DN	-0.8871	2.6049E-03	4.9300E-05	-1.7236E-04	16.7724	6.0722E-04	0.0160	2.3010E-05
	POA	N	-1.1752	3.2554E-03	3.6000E-05	-1.6699E-04	23.0000	1.0000E-04	0.0136	5.8950E-03
		DN	-1.1279	3.3438E-03	5.0455E-05	-1.7222E-04	16.2032	7.4086E-04	0.0158	9.2326E-06

Moreover, Figure 15 provides a convergence curves graph of eight algorithms under noised data and denoised data, which indicates that RMSE obtained by denoised data is smaller

than RMSE obtained by noised data. Particularly, POA owns the smallest RMSE while MFO and IWOA prematurely converge to local optimum which means the great global searching ability of POA. While MVO, GWO, JS, MFO, and TLBO can obtain almost the same accuracy from noise data with POA, POA enjoys the most remarkable precision from denoised data. Meanwhile, POA owns the best performance among the eight algorithms.

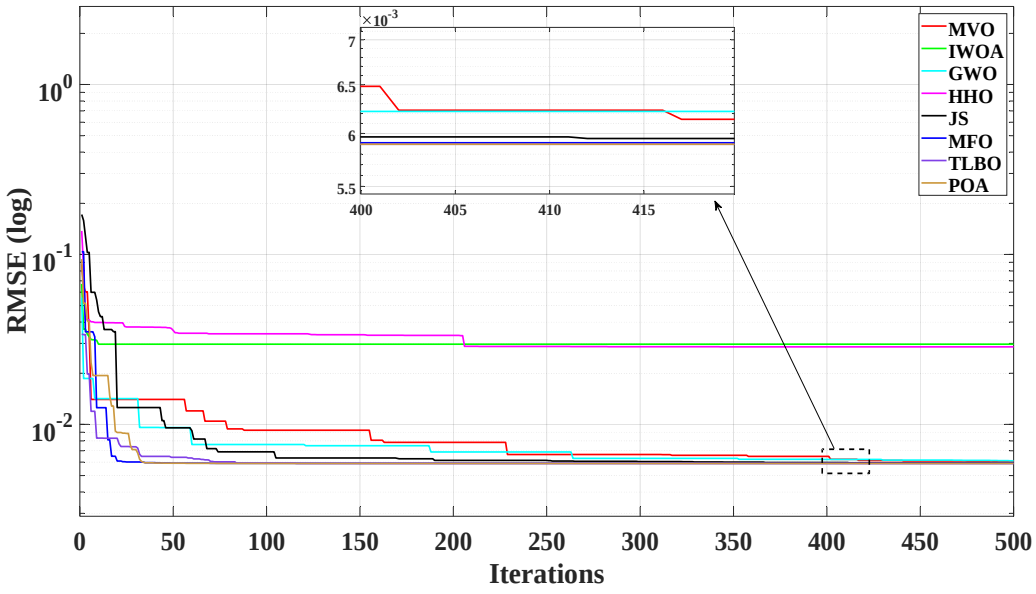

(a)

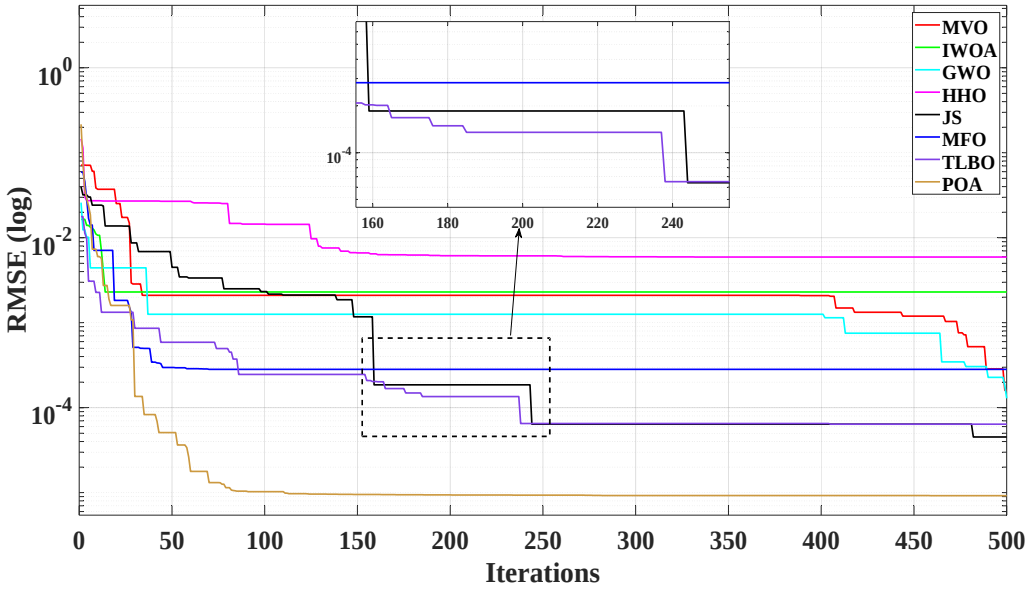

(b)

Fig. 15. Convergence curves of RMSE obtained by MhAs under MTMP: (a) noised data and (b) denoised data.

Boxplot of eight algorithms is shown in Fig. 16, which illustrates that RMSE obtained by denoised data has a smaller distribution range and upper/lower bounds compared with RMSE obtained by noise data. From it, it can be concluded that every algorithm can find a satisfied outcome under different data except for HHO and GWO, but express different degrees of stability. Particularly, based on denoised data, POA has more satisfied results than other algorithms, which means the most suitable parameters can be obtained by POA.

Moreover, Table 9 shows the statistical results of RMSE obtained by denoised data under MTMP. It illustrates that POA can obtain more stable results compared with other algorithms, for example, minimum, median, mean, maximum, and SD of RMSE. Meanwhile, the measurement indicators of the other seven algorithms have a certain gap with that of POA. Therefore, it can be simply summarized that POA owns the most satisfactory performance under MTMP.

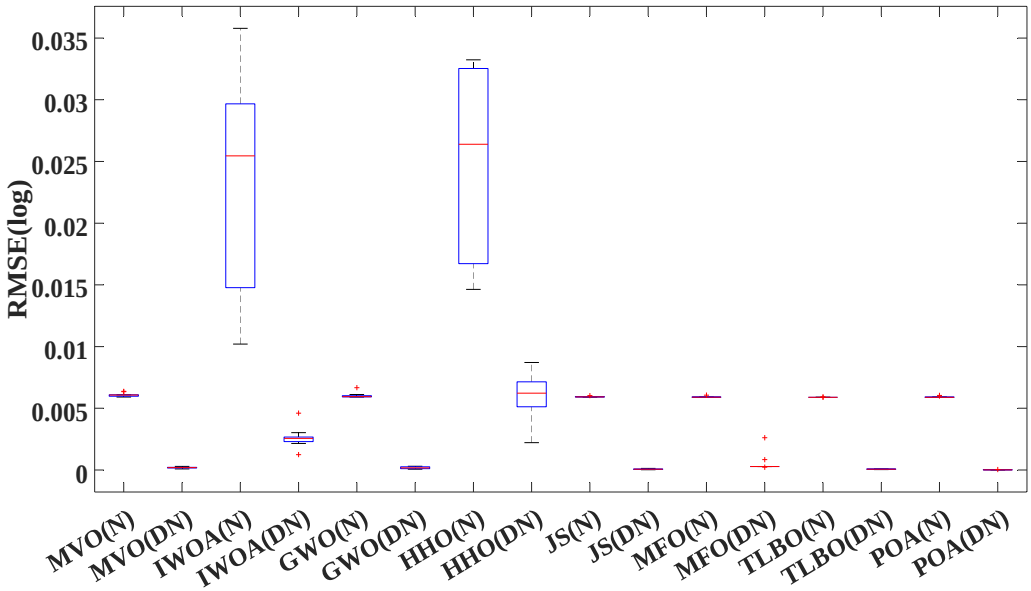

Fig. 16. Boxplot of RMSE obtained by eight MhAs under MTMP.

Table 9. Statistical results of RMSE obtained by denoised data.

Algorithm	RMSE				
	Min.	Median	Mean	Max.	SD
MVO	9.1120E-05	1.9497E-04	1.9506E-04	2.8883E-04	5.8333E-05
IWOA	1.2483E-03	2.5617E-03	2.6216E-03	4.6093E-03	8.4065E-04
GWO	6.6746E-05	1.7680E-04	1.8251E-04	3.0541E-04	8.7733E-05
HHO	2.2146E-03	6.2307E-03	5.9240E-03	8.7126E-03	1.8683E-03
JS	1.8714E-05	6.9333E-05	6.8882E-05	1.2675E-04	3.0031E-05
MFO	2.2813E-04	2.8247E-04	5.6620E-04	2.6155E-03	7.4179E-04
TLBO	3.6265E-05	6.5834E-05	6.7620E-05	8.5331E-05	1.4171E-05
POA	9.2326E-06	1.5205E-05	1.7425E-05	4.2055E-05	9.6879E-06

Figure 17 presents the *V-I* characteristic curve of the POA with the best performance in optimizing the denoised data under MTMP. It can be seen that the curve of fitting data practically coincides with the curve of actual data. Besides, the error measured by RMSE is equal to 99.23%, which is the sum of error between 25 sets of *V-I* data inversely derived from the identification results and the measured data. It can be condensed that the identified results of POA can match the unknown parameters in practical applications.

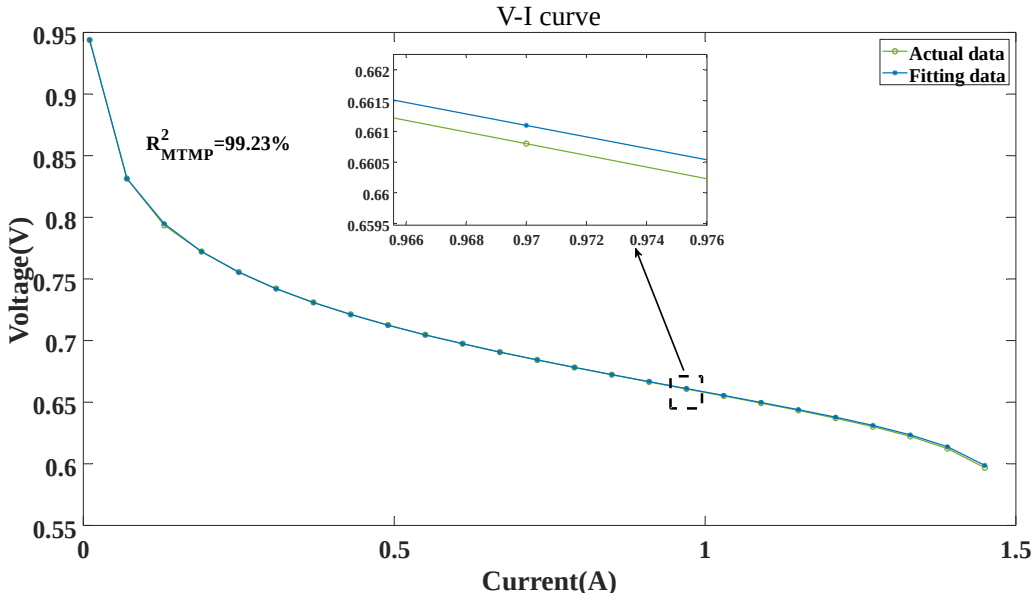

Fig. 17. FNN for *V-I* curve fitting based on denoised data under MTMP of POA.

4.4.2 Predicted data

The parameter identification results of MhAs for original data and predicted data are tabulated in Table 10. Here, it can be seen that RMSE is better after predicting, indicating that predicting data not only can obtain better parameters. Especially, based on predicted data, POA has the smallest RMSE, followed by TLBO, MFO, JS, GWO, MVO, IWOA, and HHO. Moreover, TLBO has a better outcome under noise data than that of POA, whereas the expression of POA is more satisfactory under denoised data than that of TLBO.

Table 10. Parameter identification results of original data and predicted data under eight MhAs.

State	Algorithms	Data	Identified parameters							RMSE
			ε_1	ε_2	ε_3	ε_4	λ	$R_c(\Omega)$	b(V)	
MTMP	MVO	O	-1.0623	3.8082E-03	9.6300E-05	-1.7277E-04	21.9203	7.9936E-04	0.0165	1.9657E-04
		P	-1.0053	3.1078E-03	5.9500E-05	-1.7294E-04	22.8452	6.1194E-04	0.0164	1.7530E-04
	IWOA	O	-08531	2.6101E-03	5.8000E-05	-1.6528E-04	10.7318	3.1731E-04	0.0139	4.2762E-03
		P	-0.8531	2.5796E-03	5.4000E-05	-1.7307E-04	10.0000	3.1003E-04	0.0136	1.7609E-03
	GWO	O	-0.9114	2.6726E-03	4.9000E-05	-1.7174E-04	11.5198	8.0000E-04	0.0148	2.1509E-04
		P	-1.1379	3.2678E-03	4.3100E-05	-1.7215E-04	12.2126	1.2234E-04	0.0149	1.5252E-04
	HHO	O	-0.9536	2.5117E-03	3.6000E-05	-1.0808E-04	10.0040	7.8532E-04	0.0379	3.0097E-02
		P	-0.9506	2.6246E-03	3.6000E-05	-1.7859E-04	10.0002	1.0000E-04	0.0136	2.6222E-03
	JS	O	-1.0013	3.1586E-03	6.4000E-05	-1.7255E-04	18.8705	1.0110E-04	0.0162	1.1904E-04
		P	-0.9908	3.1358E-03	6.4600E-05	-1.7242E-04	18.3654	5.0319E-04	0.0162	8.3019E-05
	MFO	O	-0.8531	3.0876E-03	8.9800E-05	-1.7202E-04	10.0000	8.0000E-04	0.0136	2.8317E-04
		P	-0.9322	3.4432E-03	9.8000E-05	-1.7251E-04	16.0541	1.0000E-04	0.0159	6.2772E-05
	TLBO	O	-0.8945	2.5043E-03	4.0900E-05	-1.7220E-04	14.1655	3.9088E-04	0.0155	6.2492E-05
		P	-0.8531	2.3127E-03	3.6200E-05	-1.7239E-04	14.7194	1.1146E-04	0.0157	5.4602E-05
	POA	O	-1.1595	3.0876E-03	8.9000E-05	-1.7208E-04	13.2260	4.2831E-04	0.0152	8.9257E-05
		P	-1.1789	3.9987E-03	8.5200E-05	-1.7230E-04	16.1010	5.3152E-04	0.0158	3.4896E-05

In addition, Figure 18 provides a convergence curves graph of MhAs, which indicates that RMSE obtained by predicted data are smaller after predicting. Particularly, POA exhibits the best performance in eight algorithms under the predicted data. It can be concluded that POA still can find high-quality solutions with high stability and can find the global optimal solution compared with the majority of algorithms.

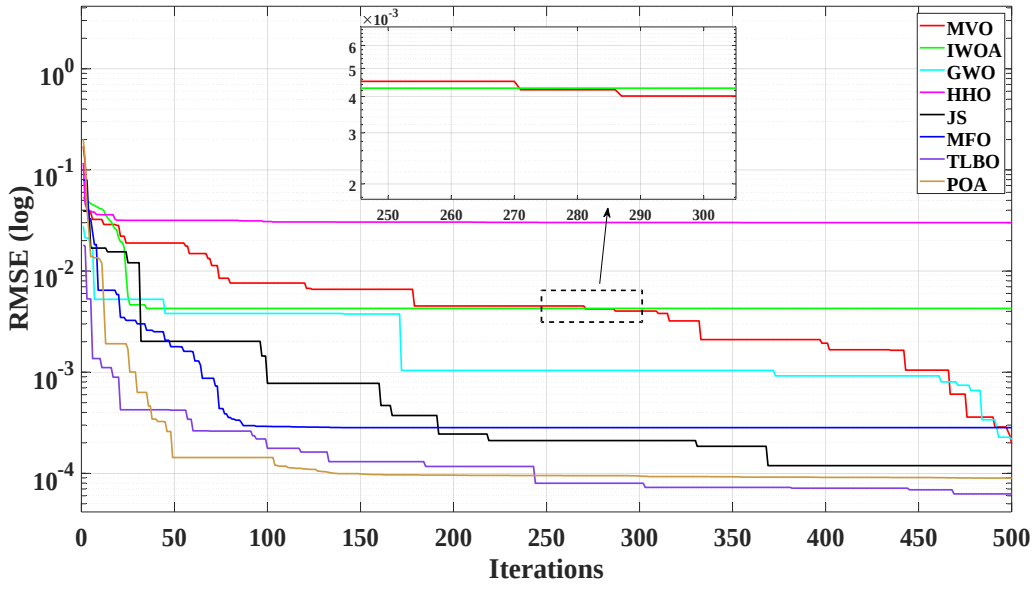

(a)

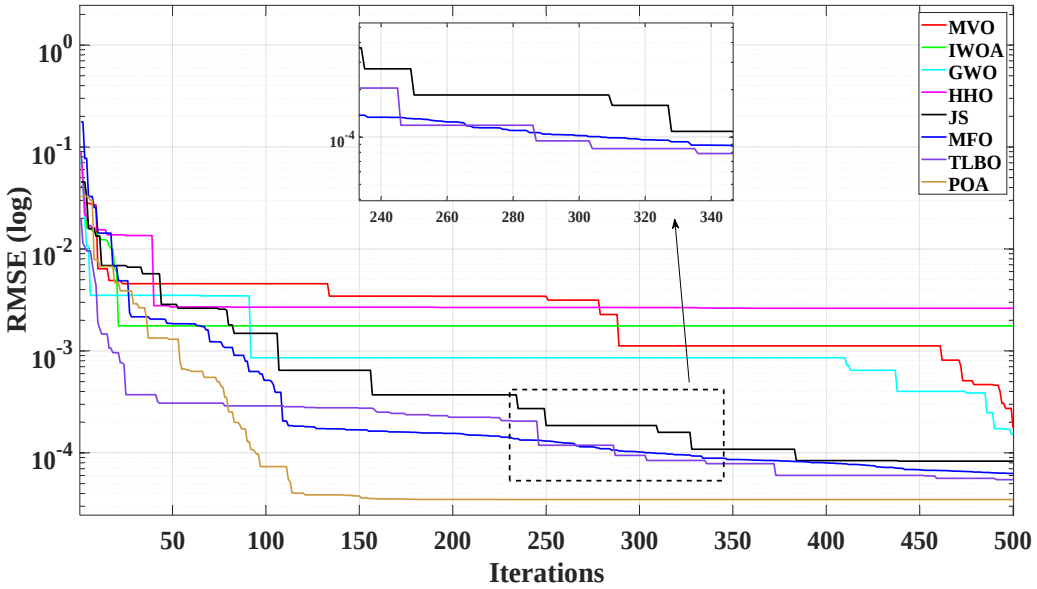

(b)

Fig. 18. Convergence curves of RMSE obtained by MhAs under MTMP: (a) original data and (b) predicted data.

Boxplot of MhAs under MTMP is given in Fig. 19, which illustrates that RMSE obtained by predicted data has a smaller distribution range and upper/lower bounds after predicting. Compared with constant algorithms, the predicted data based on boxplot of POA enjoys better performance, which demonstrates POA can search for the most suitable parameters with the highest stability.

Besides, Table 11 shows the statistical results of RMSE obtained by eight algorithms

which illustrates that POA can obtain more stable results compared with other algorithms. The RMSE of POA from predicted data has a smaller distribution range and upper/lower bounds compared with the other seven algorithms. Therefore, the predicted data contribute to better identification results, and POA owns the most stable performance under MTMP.

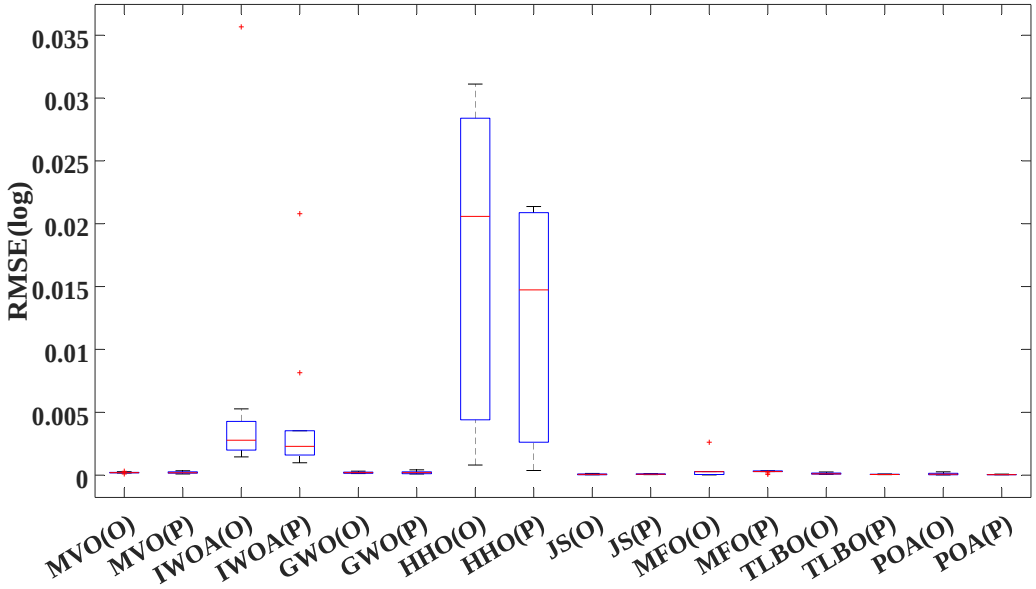

Fig. 19. Boxplot of RMSE obtained by eight MhAs under MTMP.

Table 11. Statistical results of RMSE obtained by predicted data.

Algorithm	RMSE				
	Min.	Median	Mean	Max.	SD
MVO	9.2114E-05	1.8595E-04	2.0074E-04	3.4481E-04	7.5134E-05
IWOA	9.8362E-04	2.2913E-03	4.5651E-03	2.0796E-02	6.0711E-03
GWO	8.9914E-05	1.9767E-04	2.0366E-04	4.1641E-04	1.0115E-04
HHO	3.7163E-04	1.4740E-02	1.2201E-02	2.1367E-02	9.1560E-03
JS	4.0641E-05	7.5593E-05	7.7153E-05	1.2624E-04	3.0599E-05
MFO	6.2772E-05	2.8636E-04	2.7287E-04	3.4831E-04	8.9134E-05
TLBO	4.1891E-05	5.3539E-05	5.8249E-05	8.8946E-05	1.6490E-05
POA	2.7089E-05	4.4185E-05	4.5245E-05	7.8157E-05	1.5892E-05

4.5 PEMFC parameter identification of LTHP

4.5.1 Noise reduction data

The parameter identification results of MhAs under noised data and denoised data are tabulated in Table 12. Here, it can be concluded that, compared with RMSE obtained from noised data, RMSE from denoised data is better. In particular, POA exhibits the best performance in eight algorithms and has the most decrease of 99.84%, whereas IWOA has a comparatively minimum reduction of 64.86%.

Table 12. Parameter identification results of noised data and denoised data under eight MhAs.

State	Algorithms	Data	Identified parameters							RMSE
			ε_1	ε_2	ε_3	ε_4	λ	$R_c(\Omega)$	b(V)	
		N	-1.1497	3.2768E-03	3.6000E-05	-1.8589E-04	19.3212	1.3725E-04	0.0136	1.2015E-02

THP	MVO	DN	-1.0645	3.0824E-03	4.3923E-05	-17153E-04	19.2758	1.4118E-04	0.0174	1.4998E-04
	IWOA	N	-0.8571	2.2182E-03	3.6000E-05	-1.4135E-05	13.4256	2.2498E-04	0.0136	2.6902E-02
		DN	-0.8531	2.2508E-03	3.6283E-05	-1.5132E-04	16.2715	2.9286E-04	0.0223	9.4536E-03
	GWO	N	-0.9863	3.5633E-03	9.3357E-05	-1.8509E-04	16.8532	1.4597E-04	0.0136	1.2021E-02
		DN	-1.1747	3.4661E-03	4.6145E-05	-1.7039E-04	10.6233	7.1209E-04	0.0145	3.9098E-04
	HHO	N	-1.1619	3.6915E-03	6.2104E-05	-1.7465E-04	13.3037	1.0000E-04	0.0228	1.6013E-02
		DN	-0.9212	2.7885E-03	5.5573E-05	-1.7329E-04	12.4271	2.6204E-04	0.0136	2.0683E-03
	JS	N	-0.9619	3.0589E-03	6.3106E-05	-1.8605E-04	21.0274	1.6613E-04	0.0136	1.2016E-02
		DN	-1.0304	3.2659E-03	6.4667E-05	-1.7101E-04	16.3800	5.8121E-04	0.0169	2.4324E-05
	MFO	N	-1.1993	4.0423E-03	7.9065E-05	-1.8588E-04	19.6314	1.0000E-04	0.0136	1.2014E-02
		DN	-1.1997	4.2060E-03	9.2999E-05	-1.7105E-04	17.6707	8.0000E-04	0.0174	2.4655E-05
	TLBO	N	-0.8551	2.3360E-03	3.6000E-05	-1.8589E-04	19.5458	1.0000E-04	0.0136	1.2014E-02
		DN	-0.8700	2.5225E-03	4.8266E-05	-1.7113E-04	15.0933	1.3602E-04	0.0168	3.3245E-05
	POA	N	-1.1770	3.9950E-03	8.0751E-05	-1.8571E-04	20.7886	6.3403E-04	0.0136	1.2017E-02
		DN	-1.1216	3.2526E-03	4.3007E-05	-1.7105E-04	16.2891	5.9691E-04	0.0169	1.9683E-05

Meanwhile, the convergence curves graph of MhAs under noised data and denoised data are demonstrated in Fig. 20, which indicates that RMSE obtained by denoised data has better performance than RMSE obtained by noised data. Besides, one can easily observe that POA can always find the global optimal solution in a more predictable way under noised data and denoised data, which can effectively reflect the superior performance of POA.

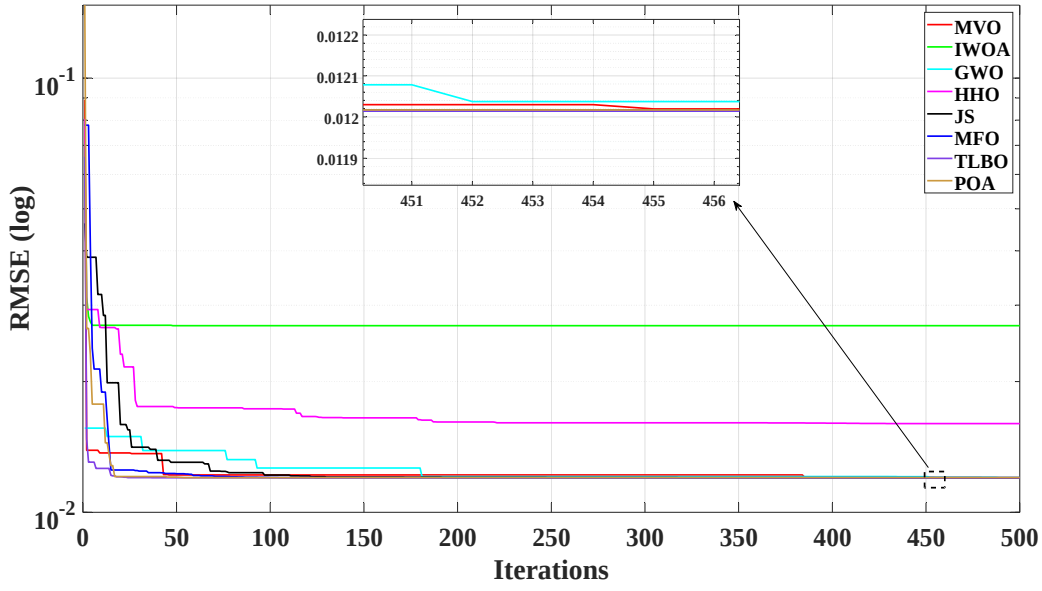

(a)

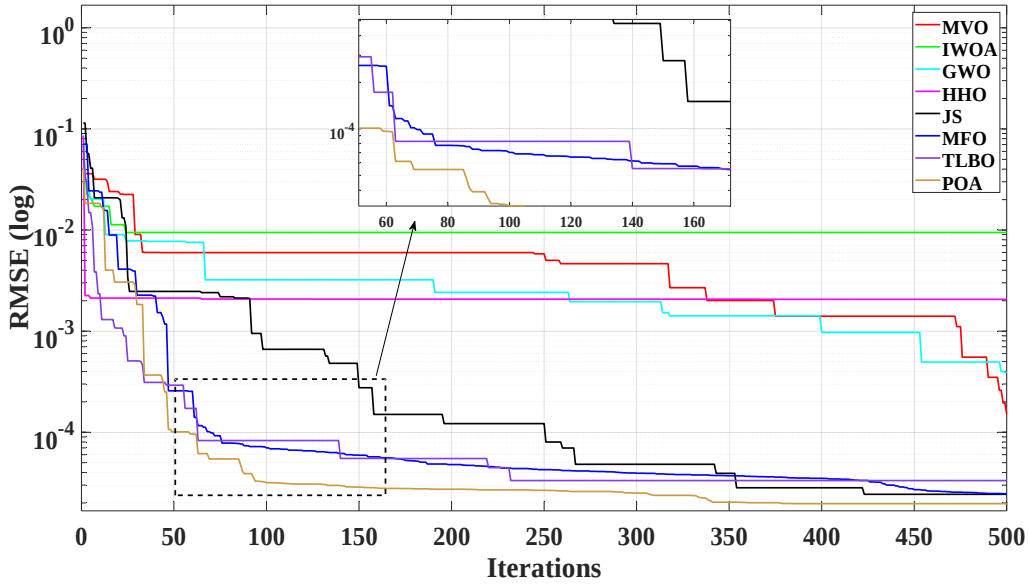

(b)

Fig. 20. Convergence curves of RMSE obtained by eight MhAs under LTHP: (a) noise data and (b) denoised data.

Figure 21 describes RMSE distribution boxplot obtained by MhAs under LTHP, which illustrates that RMSE obtained by noised data have worse distribution range and upper/lower bounds compared with RMSE obtained by denoised data. Compared with constant algorithms, the denoised data based on boxplot of POA enjoys the smallest distribution range and lowest upper/lower bounds, which illustrates POA can search for the most suitable parameters with the highest stability.

Furthermore, Table 13 shows statistical results of RMSE which illustrates that POA performs better than other algorithms in terms of minimum, mean, maximum, and SD of RMSE. It can be summarized that the preprocessing of FNN can obtain better identification results and POA owns the best performance under LTHP.

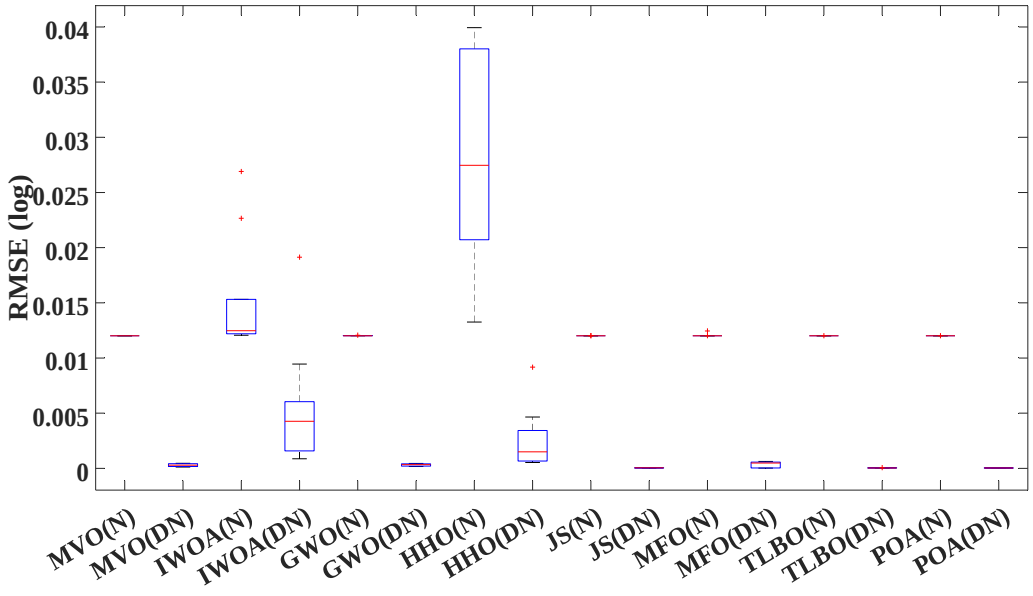

Fig. 21. Boxplot of RMSE obtained by eight MhAs under LTHP.

Table 13. Statistical results of RMSE obtained by denoised data.

Algorithm	RMSE				
	Min.	Median	Mean	Max.	SD
MVO	1.2351E-04	2.9233E-04	2.9503E-04	4.6257E-04	1.2729E-04
IWOA	8.7035E-04	4.2619E-03	5.3895E-03	1.9140E-02	5.5438E-03
GWO	1.7038E-04	3.3743E-04	3.1172E-04	4.4351E-04	1.0635E-04
HHO	5.2724E-04	1.4965E-03	2.4960E-03	9.1707E-03	2.7238E-03
JS	2.4324E-05	4.7189E-05	4.6337E-05	6.6975E-05	1.3759E-05
MFO	2.0177E-05	4.7934E-04	3.7621E-04	6.3240E-04	2.5326E-04
TLBO	2.5656E-05	3.6863E-05	3.9960E-05	6.3730E-05	1.2265E-05
POA	1.9683E-05	3.7831E-05	3.5327E-05	4.8693E-05	1.0147E-05

Figure 22 illustrates *V-I* curve obtained by POA with the denoised data. It can be noticed that the curve of noise reduction data practically matched up with the curve of actual data. Meanwhile, the error measured by RMSE is equal to 98.58%, which is the sum of error between 25 sets of *V-I* data inversely derived from the identification results and the measured data.

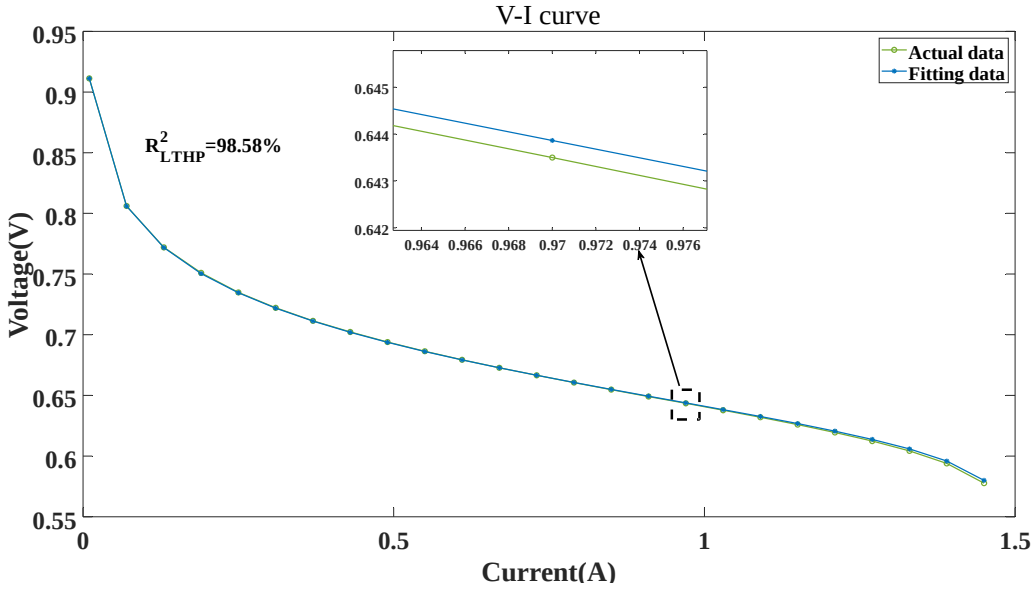

Fig. 22. FNN for *V-I* curve fitting based on denoised data under LTHP of POA.

4.5.2 Predicted data

Table 14 makes a list of the parameter identification results of MhAs for original data and predicted data. Here, it can be noticed that RMSE obtained by predicted data is better than RMSE obtained by original data, indicating that predicted data can obtain better parameters and that the preprocessing of FNN has a significant advantage. Especially, based on predicted data, POA has the smallest RMSE, followed by JS, TLBO, GWO, MVO, MFO, IWOA, and HHO. Meanwhile, under predicted data, the RMSE of the POA is far more than that of other algorithms, which means POA enjoys excellent identification accuracy.

Table 14. Parameter identification results of original data and predicted data under eight MhAs.

State	Algorithms	Data	Identified parameters							RMSE
			ε_1	ε_2	ε_3	ε_4	λ	$R_c(\Omega)$	b(V)	
		O	-0.8792	2.5251E-03	4.6331E-05	-1.7055E-04	10.0601	1.2508E-04	0.0142	3.9376E-04

LTHP	MVO	P	-09150	3.2415E-03	8.9119E-05	-1.7030E-04	10.7794	4.4988E-04	0.0145	3.4810E-04
	IWOA	O	-0.8531	2.1653E-03	3.6000E-05	-9.5400E-05	10.0000	1.8395E-04	0.0363	3.2885E-02
		P	-0.8531	2.5047E-03	5.1270E-05	-1.7103E-04	16.5240	1.2139E-04	0.0165	1.3135E-03
	GWO	O	-0.8941	2.5711E-03	4.6251E-05	-1.7037E-04	10.1323	6.2562E-04	0.0140	4.4090E-04
		P	-0.9981	2.7706E-03	3.6776E-05	-1.7183E-04	17.7248	1.0868E-04	0.0172	1.8430E-04
	HHO	O	-0.8936	2.3156E-03	3.6005E-05	-9.9975E-05	10.0014	2.7566E-04	0.0398	3.1408E-02
		P	-0.8531	2.2727E-03	3.6004E-05	-1.6226E-04	10.0012	7.0934E-04	0.0149	2.1794E-03
	JS	O	-1.0513	3.3057E-03	6.2746E-05	-1.7131E-04	19.3205	5.9454E-04	0.0174	1.0010E-04
		P	-1.0781	3.2024E-03	4.9217E-05	-1.7100E-04	16.1684	5.8397E-04	0.0169	5.7688E-05
	MFO	O	-1.1997	3.4904E-03	4.2224E-05	-1.7062E-04	10.0000	8.0000E-04	0.0136	5.6756E-04
		P	-0.9512	2.6076E-03	3.6000E-05	-1.6987E-04	10.0000	8.0000E-04	0.0136	4.7282E-04
	TLBO	O	-0.8535	2.5424E-03	5.3394E-05	-1.7085E-04	13.2480	1.4049E-04	0.0163	1.5563E-04
		P	-0.8946	2.4720E-03	3.9096E-05	-1.7113E-04	14.7221	3.9393E-04	0.0165	8.0660E-05
	POA	O	-0.9717	2.6789E-03	3.6322E-05	-1.7077E-04	12.9917	3.3420E-04	0.0161	1.4692E-04
		P	-0.8851	2.7882E-03	6.3684E-05	-1.7105E-04	15.6807	5.1874E-04	0.0168	4.8399E-05

Moreover, Figure 23 provides a convergence curves graph of MhAs under original data and predicted data, which characterizes that RMSE obtained by predicted data has a better performance compared with RMSE from original data. Under the original data case, MFO can rapidly find the globally optimal solution to reduce RMSE, followed by POA. One can easily notice that POA has a relatively excellent optimization ability compared with the majority of algorithms. Meanwhile, JS shows better identification results than POA in continuous iteration from original data, but POA expresses better discernment and speed under predicted data.

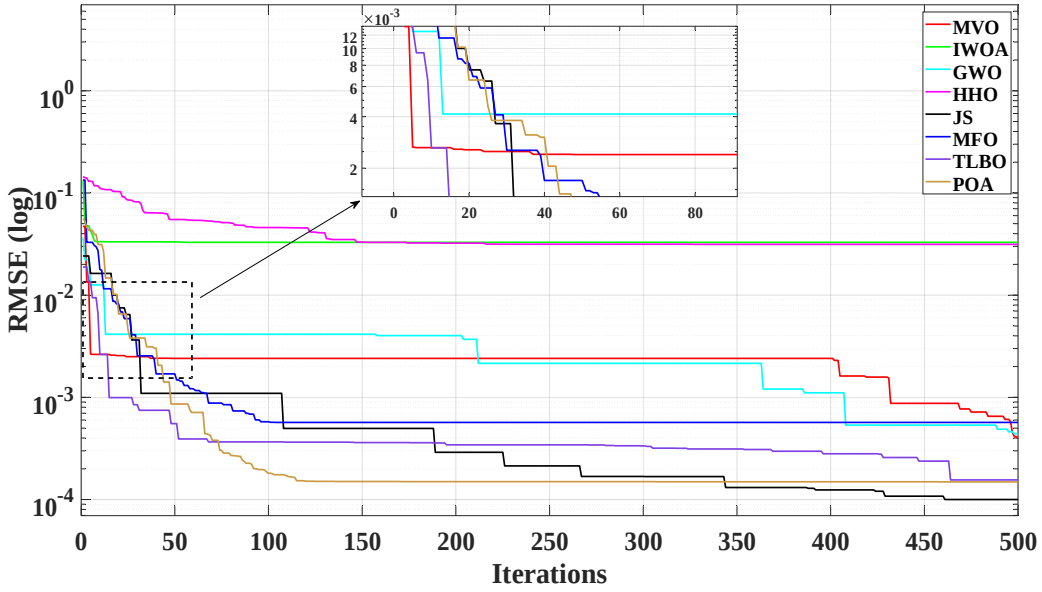

(a)

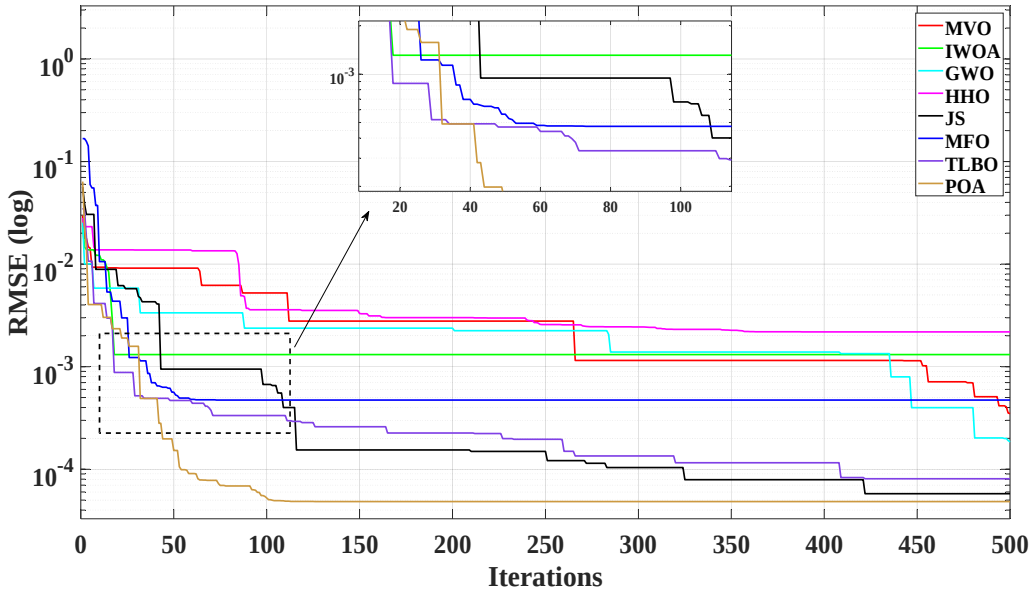

(b)

Fig. 23. Convergence curves of RMSE obtained by eight MhAs under LTHP: (a) original data and (b) predicted data.

Figure 24 describes RMSE distribution boxplot obtained by MhAs under LTHP, which illustrates that RMSE obtained by predicted data have a better distribution range and upper/lower bounds. Especially, based on predicted data, POA enjoys the satisfied performance among MhAs, which means the most suitable parameters can be obtained by POA.

Moreover, Table 15 represents the statistical results of RMSE obtained by eight algorithms which illustrates that POA has the best performance. Therefore, it can be simply summarized that POA can achieve the most satisfactory optimization ability under LTHP.

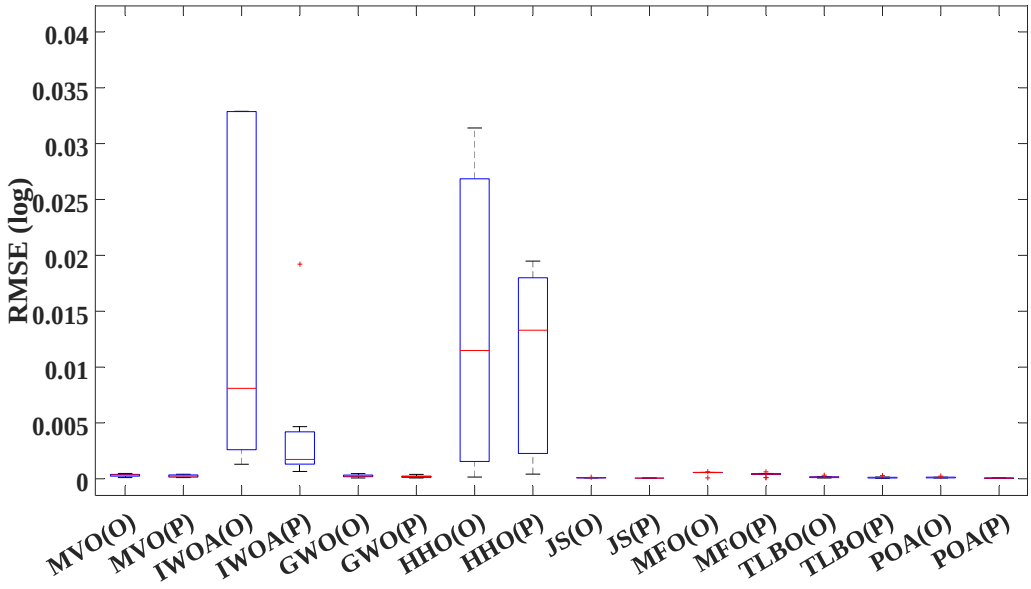

Fig. 24. Boxplot of RMSE obtained by eight MhAs under LTHP.

Table 15. Statistical results of RMSE obtained by predicted data.

Algorithm	RMSE				
	Min.	Median	Mean	Max.	SD

MVO	1.0935E-04	2.4687E-04	2.4977E-04	4.1061E-04	1.1192E-04
IWOA	6.5260E-04	1.7363E-03	3.9221E-03	1.9212E-02	5.5378E-03
GWO	6.8106E-05	2.0358E-04	2.0813E-04	3.9057E-04	1.0202E-04
HHO	4.2381E-04	1.3302E-02	1.1355E-02	1.9485E-02	7.5894E-03
JS	4.8378E-05	5.8476E-05	5.8474E-05	7.0743E-05	7.1916E-06
MFO	3.9941E-05	2.5976E-04	2.5238E-04	4.7282E-04	1.9331E-04
TLBO	5.3577E-05	1.1373E-04	1.2028E-04	2.8712E-04	6.7266E-05
POA	4.6706E-05	5.6578E-05	5.6593E-05	6.9646E-05	8.0560E-06

5. Discussion

As the inherent searching randomness of MhAs, it is hard for FNN-POA to always obtain the optimal results or exhibit the obvious outperformance compared with other methods. For instance, FNN-POA applied in predicted data performs a similar performance with FNN-MFO in Fig. 14 and FNN-TLBO in Fig. 19.

For a more comprehensive comparison of the optimization performance of various algorithms, Figure 25 intuitively illustrates radar graphs regarding five aspects of RMSE, i.e., the minimum, median, mean, maximum, and SD. Note that the best performer is rated at 8 scores and then decreased by 1 score in turn, which means the highest total score and the lowest total score are 40 and 8, respectively. Besides, the higher the total score is, the bigger the area of the radar graph will be. From the radar graphs, one can easily observe that POA always acquires the highest total score and biggest area under different operating conditions compared with other competitive algorithms. In particular, its scores are 38, 40, and 39 under HTLP, MTMP, and LTHP operating conditions, respectively. Similar results can also be obtained based on predicted data, as shown in Fig. 26. Consequently, POA remarkably outperforms other algorithms in the comprehensive performance of parameter identification. In conclusion, after data is preprocessed by FNN, POA can obtain a more satisfactory performance than other algorithms, which significantly demonstrates the powerful searching ability and optimization accuracy of FNN-POA.

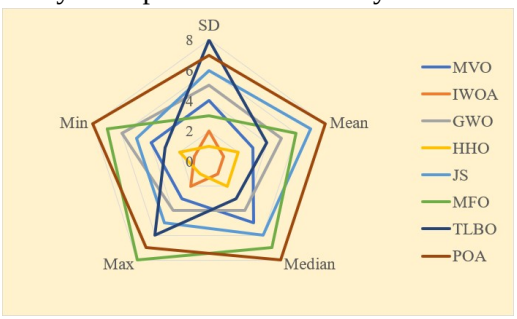

(a)

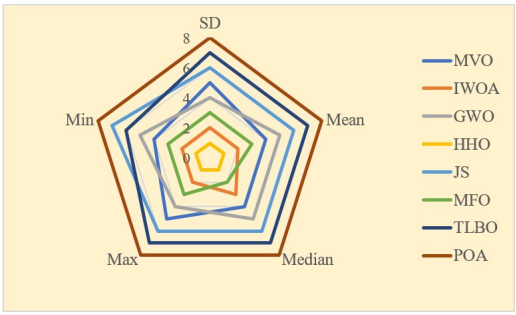

(b)

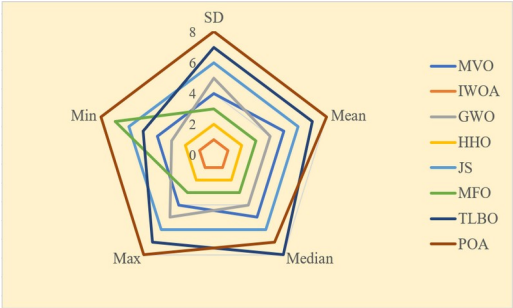

(c)

Fig. 25. Radar graphs obtained by denoised data under three operating conditions: (a) HTLP; (b) MTMP; and (c) LTHP.

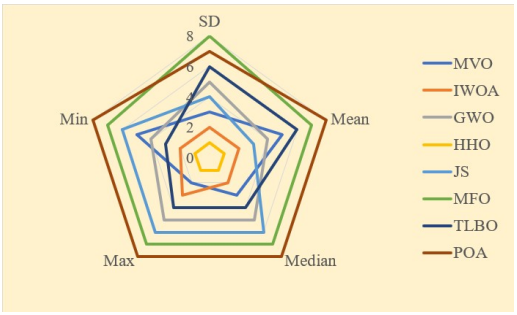

(a)

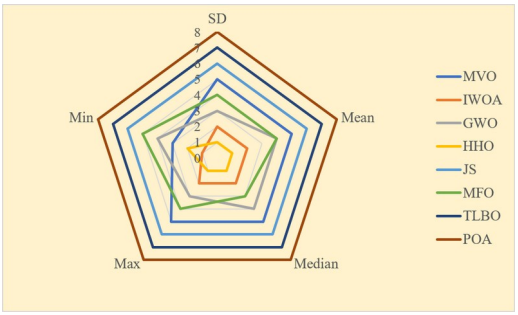

(b)

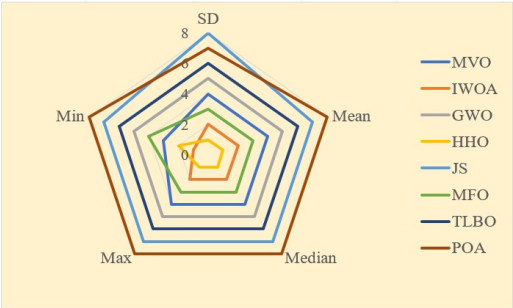

(c)

Fig. 26. Radar graphs obtained by predicted data under three operating conditions: (a) HTLP; (b) MTMP; and (c) LTHP.

6. Conclusion

This paper proposes an intelligent parameter identification method for PEMFC via FNN-POA. According to thorough case studies, five conclusions can be summarized as follows:

- While the traditional MhAs based PEMFC parameter identification methods are easy to induce low-quality optimization results under the influence of insufficient data and noise data, FNN based data preprocess model which has better performance than BP, GRNN, and LSTM can help them obtain more ideal results;
- Both Gaussian white noise and Rayleigh white noise with three SNR levels (i.e., 20 dB, 25 dB, and 35 dB) are introduced to simulate various disturbances. The outstanding performance of FNN in noise reduction is thoroughly validated by these noise;

- POA outperforms the others most of the time, only underperforming TLBO under LTHP and MFO under HTLP when the original data. Therefore, POA can carry out more effective global exploration and local development for PEMFC parameter identification;
- Case studies demonstrate that FNN-POA can not only enhance optimization ability and precision but also possess high robustness and optimization quality. In particular, RMSE obtained by FNN-POA is reduced by 96.45%, 99.44%, and 99.84% respectively under HTLP, MTMP, and LTHP through noise reduction. Meanwhile, RMSE obtained by FNN-POA is decreased by 41.79%, 60.72%, and 67.66% under HTLP, MTMP, and LTHP through data expansion.

In the end, during PEMFC operation, FNN-POA can efficiently and accurately identify unknown parameters even in harsh environments, i.e., data loss and the effect of ambient temperature. FNN-POA framework gives an important guideline for parameter identification of PEMFC single model. It may not be confined to itself, which could also be applied to PEMFC stack model as well as other fuel cells and even PV cells.

Declaration of Competing Interest

The authors declare that they have no known competing financial interests or personal relationships that could have appeared to influence the work reported in this paper.

Acknowledgments

This work is supported by the National Natural Science Foundation of China (62263014), the Yunnan Provincial Basic Research Project (202201AT070857), and China Scholarship Council.

Reference

[1] Miao C R, Wang Q, Tang, Y. A multi-energy inertia-based power support strategy with gas network constraints. *Protection and Control of Modern Power Systems*, **2023**, 8(1): 18.

[2] Chen Y J, Yang B, Guo Z X, et al. Dynamic reconfiguration for TEG systems under heterogeneous temperature distribution via adaptive coordinated seeker. *Protection and Control of Modern Power Systems*, **2022**, 7(38): 1-19.

[3] Wang Y T, Yang B. Optimal PV array reconfiguration under partial shading condition through dynamic leader based collective intelligence. *Protection and Control of Modern Power Systems*, **2023**, 8(1): 1-16.

[4] Yang B, Liu B Q, Zhou HY, et al. A critical survey of technologies of large offshore wind farm integration: summarization, advances, and perspectives. *Protection and Control of Modern Power*

Systems, **2022**, 7(17): 1-32.

[5] Rosen M A, Koohi-Fayegh S. The prospects for hydrogen as an energy carrier: an overview of hydrogen energy and hydrogen energy systems. *Energy, Ecology and Environment*, **2016**, 1: 10-29.

[6] Ferriday T B, Middleton P H. Alkaline fuel cell technology-a review. *International Journal of Hydrogen Energy*, **2021**, 46(35): 18489-18510.

[7] Zhang H C, Lin G X, Chen J C. Multi-objective optimisation analysis and load matching of a phosphoric acid fuel cell system. *International Journal of Hydrogen Energy*, **2012**, 37(4): 3438-3446.

[8] Yang B, Zeng C Y, Wang L, et al. Parameter identification of proton exchange membrane fuel cell via Levenberg-Marquardt backpropagation algorithm. *International Journal of Hydrogen Energy*, **2021**, 46(44): 22998-23012.

[9] Antolini E. The stability of molten carbonate fuel cell electrodes: a review of recent improvements. *Applied Energy*, **2011**, 88(12): 4274-4293.

[10] Yang B, Li Y L, Li J L, et al. Comprehensive summarization of solid oxide fuel cell control: a state-of-the-art review. *Protection and Control of Modern Power Systems*, **2022**, 7(36): 1-31.

[11] Min X T, Chai D, Ding K P, et al. Hydrogen generation by hydrolysis of solid sodium borohydride for portable PEMFC applications. *Fuel*, **2023**, 350: 128777.

[12] Bahari M, Rostami M, Entezari A, et al. Performance evaluation and multi-objective optimization of a novel UAV propulsion system based on PEM fuel cell. *Fuel*, **2022**, 311: 122554.

[13] Sahraoui M, Bichioui, Y, Halouani K. Three-dimensional modeling of water transport in PEMFC. *International Journal of Hydrogen Energy*, **2013**, 38(20): 8524-8531.

[14] Rao Y, Shao Z, Ahangarnejad A H, et al. Shark smell optimizer applied to identify the optimal parameters of the proton exchange membrane fuel cell model. *Energy Conversion and Management*, **2019**, 182: 1-8.

[15] Selem S I, Hasanien H M, El-Fergany A A. Parameters extraction of PEMFC's model using manta rays foraging optimizer. *International Journal of Energy Research*, **2020**, 44(6): 4629-4640.

[16] Wang C S, Nehrir M H, Shaw S R. Dynamic models and model validation for PEM fuel cells using electrical circuits. *IEEE Transactions on Energy Conversion*, **2005**, 20(2): 442-451.

[17] Yang B, Wang J B, Yu L, et al. A critical survey on proton exchange membrane fuel cell parameter estimation using meta-heuristic algorithms. *Journal of Cleaner Production*, **2020**, 265: 121660.

[18] Salim R, Nabag M, Noura H, et al. The parameter identification of the Nexa 1.2 kW PEMFC's model using particle swarm optimization. *Renewable Energy*, **2015**, 82: 26-34.

[19] Rezk H, Ferahtia S, Djeroui A, et al. Optimal parameter estimation strategy of PEM fuel cell using gradient-based optimizer. *Energy*, **2022**, 239: 122096.

[20] Gouda E A, Kotb M F, El-Fergany A A. Jellyfish search algorithm for extracting unknown parameters of PEM fuel cell models: steady-state performance and analysis. *Energy*, **2021**, 221: 119836.

[21] Fathy A, Rezk H. Multi-verse optimizer for identifying the optimal parameters of PEMFC model. *Energy*, **2018**, 143: 634-644.

[22] Askarzadeh A, Rezazadeh A. A new heuristic optimization algorithm for modeling of proton exchange membrane fuel cell: bird mating optimizer. *International Journal of Energy Research*, 2013, 37(10): 1196-1204.

[23] Ashraf H, Abdellatif S O, Elkholy M M, et al. Honey badger optimizer for extracting the ungiven parameters of PEMFC model: steady-state assessment. *Energy Conversion and Management*,

2022, 258: 115521.

[24] Zhu Y L, Yousefi, N. Optimal parameter identification of PEMFC stacks using adaptive sparrow search algorithm. *International Journal of Hydrogen Energy*, **2021**, 46(14): 9541-9552.

[25] Bao S J, Ebadi A, Toughani M, et al. A new method for optimal parameters identification of a PEMFC using an improved version of Monarch butterfly optimization algorithm. *International Journal of Hydrogen Energy*, **2020**, 45(35): 17882-17892.

[26] Daud W R W, Rosli R E, Majlan E H, et al. PEM fuel cell system control: a review. *Renewable Energy*, **2017**, 113: 620-638.

[27] Arif M, Cheung S C, Andrews J. A systematic approach for matching simulated and experimental polarization curves for a PEM fuel cell. *International Journal of Hydrogen Energy*, **2020**, 45(3): 2206-2223.

[28] Yang B, Li D Y, Zeng C Y, et al. Parameter extraction of PEMFC via Bayesian regularization neural network based meta-heuristic algorithms. *Energy*, **2021**, 228: 120592.

[29] Priya K, Sathishkumar K, Rajasekar N. A comprehensive review on parameter estimation techniques for proton exchange membrane fuel cell modelling. *Renewable and Sustainable Energy Reviews*, **2018**, 93, 121-144.

[30] Ramsami P, Oree V. A hybrid method for forecasting the energy output of photovoltaic systems. *Energy Conversion and Management*, **2015**, 95: 406-413.

[31] Ćalasan M, Aleem S H E A, Zobaa A F. On the root mean square error (RMSE) calculation for parameter estimation of photovoltaic models: a novel exact analytical solution based on Lambert W function. *Energy conversion and management*, **2020**, 210: 112716.

[32] Chen X, Ding K, Yang H, et al. Research on real-time identification method of model parameters for the photovoltaic array. *Applied Energy*, **2023**, 342: 121157.

[33] Ojha V K, Abraham A, Snášel V. Metaheuristic design of feedforward neural networks: a review of two decades of research. *Engineering Applications of Artificial Intelligence*, **2017**, 60: 97-116.

[34] Apicella A, Donnarumma F, Isgrò F, et al. A survey on modern trainable activation functions. *Neural Networks*, **2021**, 138: 14-32.

[35] Trojovský P, Dehghani M. Pelican optimization algorithm: a novel nature-inspired algorithm for engineering applications. *Sensors*, **2022**, 22(3): 855.

[36] Alamir N, Kamel S, Megahed T F, et al. Developing hybrid demand response technique for energy management in microgrid based on pelican optimization algorithm. *Electric Power Systems Research*, **2023**, 214: 108905.

[37] Liu W, Guo Z Q, Wang D, et al. Improved whale optimization algorithm and its weights and thresholds optimization in shallow neural architecture search. *Control and Decision*, **2023**, 38(4): 1144-1152.

[38] Mirjalili S, Mirjalili S M, Lewis A. Grey wolf optimizer. *Advances in Engineering Software*, **2014**, 69: 46-61.

[39] Tayab U B, Zia A, Yang F W, et al. Short-term load forecasting for microgrid energy management system using hybrid HHO-FNN model with best-basis stationary wavelet packet transform. *Energy*, **2020**, 203: 117857.

[40] Allam D, Yousri D A, Eteiba M B. Parameters extraction of the three diode model for the multi-crystalline solar cell/module using moth-flame optimization algorithm. *Energy Conversion and Management*, **2016**, 123: 535-548.

[41] Uzlu E, Kankal M, Akpınar A, et al. Estimates of energy consumption in Turkey using neural

networks with the teaching-learning-based optimization algorithm. *Energy*, **2014**, 75: 295-303.

[42] Kler D, Rana K P, Kumar V. Parameter extraction of fuel cells using hybrid interior search algorithm. *International Journal of Energy Research*, **2019**, 43(7): 2854-2880.

[43] El-Fergany A. A. Extracting optimal parameters of PEM fuel cells using salp swarm optimizer. *Renewable Energy*, **2018**, 119: 641-648.